

1 **Application of a global nonhydrostatic model with a**
2 **stretched-grid system to regional aerosol simulations**
3 **around Japan**

4

5 **D. Goto^{*1}, T. Dai^{2,3}, M. Satoh^{3,4}, H. Tomita^{4,5}, J. Uchida³, S. Misawa³, T.**
6 **Inoue³, H. Tsuruta³, K. Ueda⁶, C. F. S. Ng⁷, A. Takami¹, N. Sugimoto¹, A.**
7 **Shimizu¹, T. Ohara¹ and T. Nakajima³**

8

9 [1] National Institute for Environmental Studies, Tsukuba, Japan

10 [2] State Key Laboratory of Numerical Modeling for Atmospheric Sciences and
11 Geophysical Fluid Dynamics, Institute of Atmospheric Physics, Chinese Academy of
12 Sciences, Beijing, China

13 [3] Japan Agency for Marine-Earth Science and Technology, Yokohama, Japan

14 [4] Atmosphere and Ocean Research Institute, University of Tokyo, Kashiwa, Japan

15 [5] Advanced Institute for Computational Science, RIKEN, Kobe, Japan

16 [6] Faculty of Engineering, Kyoto University, Kyoto, Japan

17 [7] Department of Human Ecology School of International Health Graduate School of
18 medicine, University of Tokyo, Tokyo, Japan

19

20 *Correspondence to: Daisuke Goto (goto.daisuke@nies.go.jp)

21 16-2 Onogawa, Tsukuba, Ibaraki 305-8506, Japan

22 Tel: +81-29-850-2899; Fax: +81-29-850-2580

23 **Abstract**

24 An aerosol-coupled global nonhydrostatic model with a stretched-grid system has been
25 developed. Circulations over the global and target domains are simulated with a single
26 model, which includes fine meshes covering the target region to calculate meso-scale
27 circulations. The stretched global model involves lower computational costs to simulate
28 atmospheric aerosols with fine horizontal resolutions compared with a global uniform
29 nonhydrostatic model, whereas it may require higher computational costs compared
30 with the general regional models, because the stretched-grid system calculates inside
31 and outside the target domain. As opposed to general regional models, the
32 stretched-grid system does require neither a nesting technique nor lateral boundary
33 conditions. In this study, we developed a new-type regional model for the simulation of
34 aerosols over Japan, especially in the Kanto areas surrounding Tokyo, with a maximum
35 horizontal resolution of approximately 10 km. This model usually reproduces temporal
36 variations and their averages of the observed weather around Japan. This model
37 generally reproduces monthly mean distributions of the observed sulfate and SO₂ over
38 East Asia, with the high correlations of more than 0.5, but the underestimation of the
39 simulated concentrations by 40%. The underestimation is mainly caused by the
40 underestimation in China and possibly by the uncertainty of the simulated precipitation
41 around Japan. In the Kanto area, this model succeeds in simulating the wind patterns
42 and the diurnal transitions around the center of the Kanto area, although it is inadequate
43 to simulate the wind patterns and the diurnal transitions at some sites located at the edge
44 of the Kanto area and surrounded on three sides by mountains, e.g., Maebashi, mainly

45 due to the insufficient horizontal resolution. This model also generally reproduces both
46 diurnal and weekly variations of the observed and/or a regional aerosol-transport model,
47 WRF-CMAQ, simulated EC, sulfate, and SO₂ concentrations in the Kanto area,
48 especially with their high correlation ($R>0.5$) at Komae/Tokyo. Although the aerosol
49 module used in this study is relatively simplified compared to the general regional
50 aerosol models, this study reveals that our proposed model with the stretched-grid
51 system can be applicable for the regional aerosol simulation.

52 **1 Introduction**

53 Aerosols can greatly affect regional air quality and contribute to global climate change
54 (Forster et al., 2007). Recently, transboundary aerosol pollution, whereby regions
55 beyond a given country's borders are affected by the aerosols generated in that country,
56 has been of increasing concern (Ramanathan et al., 2008; Yu et al., 2012). The ongoing
57 rapid economic growth in developing countries has the potential to exacerbate this issue
58 (UNEP and WMO, 2011). Air pollution generated by aerosols is a critical public health
59 issue due to the deleterious effects of these particles on human health (Dockery et al.,
60 1993; Pope et al., 2009). Aerosols, which scatter and absorb solar radiation and act as
61 cloud condensation nuclei, can directly and indirectly change the Earth's radiation
62 budget. The majority of aerosols are emitted from localized areas, which are referred to
63 as hotspots, such as megacities and biomass-burning regions, and are spread throughout
64 the world via atmospheric transport (e.g., Ramanathan et al., 2008). Therefore, global
65 aerosol-transport models should consider the important regional-scale characteristics of
66 aerosol hotspots to reliably estimate their impacts on air quality and climate change.

67 Most existing global aerosol-transport models do not address the spatial variability of
68 aerosols in the vicinity of hotspots due to their coarse horizontal resolution of 100–300
69 km (Kinne et al., 2006; Textor et al., 2006). In addition, global aerosol-transport models
70 with coarse resolutions frequently adopt a spectral transform method with a hydrostatic
71 approximation to effectively calculate atmospheric dynamics. This spectral transform
72 method is less effective than the grid-point method (Stuhne and Peltier, 1996; Taylor et

73 al., 1997; Randall et al., 2000) for high horizontal resolutions (Tomita et al., 2008).
74 Models that employ the grid-point method flexibly define grid points to enable an
75 adaptive focus on study regions. Thus, global models based on the grid-point method
76 seem most appropriate for use in simulating aerosol transport from hotspots to outflow
77 regions.

78 For this purpose, we utilized the global Nonhydrostatic Icosahedral Atmospheric Model
79 (NICAM) developed by Tomita and Satoh (2004) and Satoh et al. (2008). NICAM has
80 been employed for the global simulation of atmospheric processes with high-resolution
81 grid spacing, whose size is comparable to the typical deep convective cloud scale.
82 Miura et al. (2007) performed a one-week computation with a horizontal resolution of
83 3.5 km using the Earth Simulator at the Japan Agency for Marine-Earth Science and
84 Technology (JAMSTEC) to successfully simulate a Madden-Julian Oscillation (MJO)
85 event. Suzuki et al. (2008) implemented an aerosol transport model named the Spectral
86 Radiation-Transport Model for Aerosol Species (SPRINTARS; Takemura et al., 2005)
87 in NICAM (we refer to this aerosol-coupled model as NICAM-SPRINTARS) and
88 performed a one-week simulation with a horizontal resolution of 7 km using the Earth
89 Simulator. Although these global, highly resolved calculations are promising with
90 regard to long-term climate simulations for decades, their requirement of vast computer
91 resources substantially limits their use in short-duration and/or case-specific simulations
92 due to the current limitations of computational resources. To overcome this limitation,
93 we adopt a compromise approach based on a new grid transformation named the

94 stretched grid system, which was developed and implemented in NICAM by Tomita
95 (2008a) for computationally effective simulations in the target region (see, also, Satoh
96 et al. 2010). We applied this approach to NICAM-SPRINTARS, which we named
97 Stretch-NICAM-SPRINTARS, to calculate aerosol transport processes with high
98 horizontal resolutions over aerosol source regions.

99 In this study, we focused on Japan, especially the Kanto region surrounding Tokyo
100 (Figure 1), because the Kanto region living more than 30 million people is one of the
101 largest megacities in the world. In Japan, a monitoring system for the air pollution, e.g.,
102 PM_{2.5} (aerosol particles with diameters less than 2.5 μm) and SO₂, has been operated
103 by the Japanese government. Inorganic ions, mainly sulfate, have been measured over
104 Japan and other Asian countries under EANET (Acid Deposition Monitoring Network
105 in East Asia; <http://www.eanet.asia/index.html>). Measurements of carbonaceous
106 aerosols were limited, with the exception of intensive measurements (Fine Aerosol
107 Measurement and Modeling in Kanto Area, FAMIKA) in the Kanto region during
108 summer 2007 (Hasegawa et al., 2008; Fushimi et al., 2011). For the model evaluation
109 using these measurements, we simulated aerosol spatial distributions during August
110 2007 using Stretch-NICAM-SPRINTARS with a horizontal resolution of approximately
111 10 km over the Kanto region. Because the model framework of
112 Stretch-NICAM-SPRINTARS is identical to that of globally uniformed grid simulation
113 (we named it Global-NICAM-SPRINTARS), with the exception of the grid
114 configuration, and involves lower computational costs than global simulations, the

115 investigation of the model performance of Stretch-NICAM-SPRINTARS can be simply
116 and effectively extended to improve the original NICAM-SPRINTARS with globally
117 uniform high resolution for near-future simulations. To evaluate aerosol simulations
118 with the stretched-grid system, in this study we also conducted
119 Global-NICAM-SPRINTARS, but with relatively low resolution (approximately 100
120 km) due to the limited computational resources. Although the model inter-comparison
121 using different modules coupled to different dynamic cores cannot clarify the reasons of
122 the difference in the results among the models (e.g., Textor et al., 2006), the model
123 intra-comparison approach, with the exception of the grid system and the spatial
124 resolution, is very meaningful to investigate impacts of the stretched-grid system on the
125 aerosol simulations. In addition, Stretch-NICAM-SPRINTARS can be a new-type
126 model that is also applicable for a regional simulation of aerosols, because it focuses on
127 a specific regional domain without require a nesting technique nor boundary conditions,
128 unlike general regional models.

129 For the model evaluation in the target Japan, we mainly focused on a representative
130 primary aerosol, i.e., elemental carbon (EC), and a representative secondary aerosol, i.e.,
131 sulfate. EC is directly emitted from anthropogenic combustion processes, and is a good
132 indicator to monitor the transport pattern. The global and regional modelings for sulfate,
133 which is formed from SO₂ in the atmosphere, are more deeply understood compared to
134 modelings for the other secondary aerosols such as nitrate and organic aerosols (e.g.,
135 Barrie et al., 2001; Holloway et al., 2008; Hallquist et al., 2009; Morino et al., 2010a,

136 2010b). In addition, sulfate is the largest contributor to the total secondary inorganic
137 aerosols (e.g., Zhang et al., 2007), and the sulfate mass concentrations are larger than
138 that the nitrate ones in August 2007 over the Kanto area (Morino et al., 2010c).
139 Originally, these basic components (EC and sulfate) are suitable for the evaluation in
140 this study, primarily because the stretched-grid system was applied to the simulations of
141 atmospheric pollutants over the land in the mid-latitude band for the first time and
142 secondly because the original SPRINTARS is more simplified compared to
143 conventional regional aerosol models.

144 This paper is organized as follows: the model framework of NICAM and SPRINTARS
145 and the experimental design are described in Section 2. We show two model results; (1)
146 Stretch-NICAM-SPRINTARS with glevel-6, in which “glevel” is the number of
147 divisions of an icosahedron used to construct the horizontal grid, (hereafter referred to
148 as the “NICAM-g6str” model) and (2) Global-NICAM-SPRINTARS with glevel-6
149 (hereafter referred to as the “NICAM-g6” model). In Section 3, the model results are
150 validated using in-situ measurements in terms of meteorological fields including
151 precipitation and aerosol species, especially EC, sulfate and SO₂. For the model
152 evaluation of chemical species, we also made use of results in a regional aerosol model,
153 the Community Multiscale Air Quality (CMAQ) driven by the Weather Research and
154 Forecasting (WRF) model named WRF-CMAQ, shown by Shimadera et al. (2013). We
155 also present the validation of total aerosol amounts, i.e., PM_{2.5}, and aerosol optical

156 product, i.e., extinction for spherical aerosols. Finally, the conclusions are summarized
157 in Section 4.

158

159 **2 Model description**

160 **2.1 Nonhydrostatic Icosahedral Atmospheric Model (NICAM)**

161 NICAM, which employs an icosahedral grid-point method with a nonhydrostatic
162 equation system (Tomita and Satoh, 2004; Satoh et al., 2008, 2014), is run with a
163 maximum horizontal resolution of 3.5 km (Tomita et al. 2005; Miura et al., 2007) and
164 can be applied to a transport model of aerosols and gases as a conventional atmospheric
165 general circulation model (Suzuki et al., 2008; Niwa et al., 2011; Dai et al., 2014a,
166 2014b; Goto, 2014). NICAM can also be employed for regional-scale simulations by
167 adopting a stretched-grid system (Tomita, 2008a; Satoh et al., 2010). The stretched
168 icosahedral grid was developed from a general grid transformation method, i.e., the
169 Schmidt transformation method, for a horizontal grid system on a sphere. In the
170 Schmidt transformation, the grid interval on a sphere lacks uniformity with a finer
171 horizontal resolution close to the center of the target region. Tomita (2008a) showed
172 that the Schmidt transformation minimizes potential errors involving the isotropy and
173 homogeneity of the target region. The stretched-grid system can solve the main
174 problems associated with commonly used regional models, which occur from artificial
175 perturbations near boundary areas in cases where meteorological and aerosol fields are
176 prescribed. In addition, the computational cost of the stretched-grid system is

177 substantially lower than that of a global calculation under the same horizontal resolution
178 in the target region. For example, when the globally uniform grid with a maximum
179 horizontal resolution of 10 km is applied to the global simulation, the minimum
180 required theoretical computational cost is 64-256 times higher than the cost of the
181 stretched-grid system in this study. Compared to conventional regional models, the
182 computational cost may increase because the stretched-grid system requires the
183 calculation outside the target domain. Furthermore, the model framework of the
184 stretched global model is identical to that of the uniformed global model without special
185 modifications, whereas the model framework of regional models is usually different
186 from that of global models. These advantages can facilitate additional developments for
187 global simulations by testing a new scheme with minimal computational cost.
188 Compared with general regional models, the stretched-grid system is more suitable for
189 the current study, which aimed to extend its use to the global uniform high-resolution
190 NICAM-SPRINTARS.

191 In this study, we adopt the stretched-grid system to focus on the Kanto region, including
192 Tokyo, using glevel-6 resolution and the stretched ratio of 100 (we call it
193 NICAM-g6str), which is the ratio of the largest horizontal grid spacing located on the
194 opposite side of the earth from Tokyo to the smallest horizontal grid spacing near
195 Tokyo. As a result, a minimum horizontal resolution of 11 km around the center
196 (140.00°E, 35.00°N) was used. NICAM implements comprehensive physical processes
197 of radiation, boundary layer and cloud microphysics. The radiation transfer model is

198 implemented in NICAM with the k-distribution radiation scheme MSTRN, which
199 incorporates scattering, absorption and emissivity by aerosol and cloud particles as well
200 as absorption by gaseous compounds (Nakajima et al., 2000; Sekiguchi and Nakajima,
201 2008). The vertical turbulent scheme comprises the level 2 scheme of turbulence closure
202 by Mellor and Yamada (1974), Nakanishi and Niino (2004, 2009) and Noda et al.
203 (2009). The cloud microphysics consist of the six-class single-moment bulk scheme
204 (water vapor, cloud water, rain, cloud ice, snowflakes and graupel) (Tomita, 2008b).
205 Based on our experience in previous studies, we did not employ cumulus
206 parameterization in this study (e.g., Tomita et al., 2005; Sato et al., 2009; Nasuno, 2013).
207 The topography used in this study is based on GTOPO30 (the horizontal resolution is 30
208 arc seconds, that is approximately 1 km) courtesy of the U.S. Geological Survey. The
209 vertical coordinates system adopts Lorenz grid and z^* (terrain-following) coordinates
210 with the 40 layers of z-levels and model top of 40 km height (Sato et al., 2008). The
211 timestep was set to 20 seconds.

212

213 **2.2 SPRINTARS**

214 Based on the approach of Suzuki et al. (2008), the three-dimensional aerosol-transport
215 model—Spectral Radiation-Transport Model for Aerosol Species (SPRINTARS;
216 Takemura et al., 2000, 2002, 2005; Goto et al. 2011a,b,c)—was coupled to NICAM in
217 this study. The SPRINTARS model calculates the mass mixing ratios of the primary
218 tropospheric aerosols, i.e., carbonaceous aerosol (EC and OC, organic carbon), sulfate,
219 soil dust, sea salt and the precursor gases of sulfate, namely, SO_2 and dimethylsulfide

220 (DMS). The aerosol module considers the following processes; emission, advection,
221 diffusion, sulfur chemistry, wet deposition and dry deposition, including gravitational
222 settling. For carbonaceous aerosols, the 50% mass of EC from fossil fuel sources is
223 composed of externally mixed particles, whereas other carbonaceous particles are
224 emitted and treated as internal mixtures of EC and OC (EC-OC internal mixture).
225 Biogenic secondary organic aerosols (SOAs) from terpenes are treated but are greatly
226 simplified by multiplying a conversion factor to the terpenes emission (Takemura,
227 2012). In addition, anthropogenic SOAs from toluene and xylene are disregarded in this
228 study. The bulk mass concentrations of EC, OC, and sulfate are calculated by
229 single-modal approach, which means that the SPRINTARS model does not explicitly
230 treat aerosol dynamic processes such as coagulation and condensation. The particle size
231 distribution of the dry particles are prescribed in a logarithmic normal size distribution
232 with dry mode radii of 18, 100, 80 and 69.5 nm, for pure EC, EC-OC internal mixture,
233 biogenic SOA and externally mixed sulfate, respectively (Goto et al., 2011a). The
234 hygroscopicities, densities and refractive indices for the aerosols are set to the same
235 values used by Takemura et al. (2002) and Goto et al. (2011a). The combinations of the
236 pre-calculated cross-sections of the extinction and simulated mixing ratios for each
237 aerosol species provide the simulated aerosol extinction coefficient for each timestep of
238 the model (Takemura et al., 2002). The sulfur chemistry in SPRINTARS considers only
239 three chemical reactions to form sulfate through gas-phase oxidation of SO_2 by
240 hydroxyl radical (OH) and aqueous-phase oxidation by ozone and hydrogen peroxide.
241 The large part of SO_2 are emitted from fossil fuel combustion, biomass burning, and

242 volcano eruption, whereas some of SO₂ are formed from the oxidation of DMS, which
243 is emitted naturally from marine phytoplanktons. The numerical solution in the
244 oxidations adopts an approximation in a quasi first-order reaction using the same
245 integrated time resolution as that of the dynamic core. The pH value in the
246 aqueous-phase is fixed at 5.6, because the SPRINTARS model treats limited ions in the
247 aqueous-phase (e.g., Takemura et al., 2000). The oxidant distributions (OH, ozone and
248 hydrogen peroxide) were offline provided by a chemical transport model. The
249 atmospheric removal of aerosols in SPRINTARS includes wet (due to rainout and
250 washout) and dry (due to turbulence and gravity) deposition processes, whereas those of
251 SO₂ only include rainout and dry deposition by turbulence. In the cloudy grid, the mass
252 fractions of sulfate out of the cloud droplets to the mass of sulfate in the grid were fixed
253 at 0.5, whereas the fractions for SO₂ were determined by Henry's law (Takemura et al.,
254 2002a). As for pure EC, EC-OC internal mixture, and biogenic SOA, the mass fractions
255 were fixed at 0.1, 0.3, and 0.3, respectively. Because the SPRINTARS model does not
256 predict the mass mixing ratio of the chemical tracers inside the clouds, it assumes that
257 the tracers inside the clouds are evaporated from the clouds at one timestep. In this
258 study, the particle mass concentrations for diameters less than 2.5 μm (defined as
259 PM_{2.5}) are calculated by summing EC, organic matter by multiplying OC by 1.6
260 (Turpin and Lim, 2001), sulfate and ammonium aerosols. Because this model cannot
261 directly predict ammonium compounds, it is assumed that all sulfate is the form of
262 ammonium sulfate, so that their concentration was estimated by multiplying the mass
263 concentration of sulfate by 0.27, which is the molar ratio of ammonium ion to

264 ammonium sulfate. The nitrate in this study is disregarded, primarily because the main
265 objective in this study is modeling of sulfate as a representative secondary aerosols and
266 secondly because the nitrate mass concentrations are lower than the sulfate ones with
267 the target of August 2007 in Japan (Morino et al., 2010c).

268

269 **2.3 Design of the experiments**

270 The target period comprises one month in August 2007, in which an intensive
271 measurement of aerosol chemical species was conducted under Project FAMIKA
272 (Hasegawa et al., 2008; Fushimi et al., 2011). The six-hour meteorological fields (wind
273 and temperature) were nudged above a height of 2 km using NCEP-FNL reanalysis data
274 (<http://rda.ucar.edu/datasets/ds083.2/>). The one-hour sea surface temperature was also
275 nudged using the NCEP-FNL data. The initial conditions were prescribed by the
276 NCEP-FNL data for the meteorological fields and the one and a half months spinup
277 results of the Stretch-NICAM-SPRINTARS model for the aerosol fields, respectively.

278 The emission inventories of anthropogenic EC, OC and SO₂ in this experiment were
279 prepared by EAGrid2000 with a horizontal resolution of 1 km over Japan (Kannari et al.,
280 2007), REAS version 2 with a horizontal resolution of 0.25° over Asia (Kurokawa et al.,
281 2013) and the AeroCom inventory with a horizontal resolution of 1° over other areas of
282 the world (Diehl et al., 2012). Because EAGrid2000 does not explicitly estimate EC and
283 OC inventories, we estimated the inventories to be consistent with those from previous
284 studies (Morino et al., 2010a,b; Chatani et al., 2011) by modifying the PM_{2.5} inventory

285 of EAGrid2000 using scaling factors of EC/PM_{2.5} and OC/PM_{2.5} based on sources.
286 These inventories of anthropogenic EC and SO₂ in 2007 are described in Figure 2. The
287 emissions of SO₂ from volcanoes in Japan, such as Miyakejima and Sakura-jima, were
288 obtained from statistical reports (<http://www.seisvol.kishou.go.jp/tokyo/volcano.html>)
289 by the Japan Meteorological Agency (JMA). In this study, the distributions of three
290 hourly averaged monthly oxidants (OH, ozone and hydrogen peroxide) were derived
291 from a global chemical transport model (CHASER) coupled to the Model for
292 Interdisciplinary Research on Climate (MIROC), named MIROC-CHASER, with the
293 spatial resolution of 2.8° by 2.8° (Sudo et al., 2002).

294 To evaluate model performances in the stretched-grid system, we also simulated
295 NICAM-SPRINTARS with the globally uniformed grid simulation in glevel-6
296 resolution (the horizontal resolution is set to 110 km and we call it NICAM-g6).
297 Global-NICAM-SPRINTARS with relatively low resolution has been applied to aerosol
298 simulations and well compared with in-situ measurements and satellite remote sensing
299 (Dai et al., 2014a; Goto, 2014). In the NICAM-g6 simulation, the cloud physics apply
300 both the prognostic Arakawa-Schubert-type cumulus convection scheme (Arakawa and
301 Schubert, 1974) and the diagnostic large-scale clouds described by Le Treut and Li
302 (1991). The large-scale cloud module is based on single moment bulk scheme for cloud
303 mixing ratio. The precipitation rate is parameterized by Berry (1967). Except for the
304 grid system and the horizontal resolution (which determines the module of the cloud
305 physics), Global-NICAM-SPRINTARS was identical to Stretch-NICAM-SPRINTARS.

306 Therefore, apart from general model inter-comparison projects including various
307 aerosol modules and dynamic cores, the comparison between NICAM-g6str and
308 NICAM-g6 led to clarify impacts of the horizontal resolution on the aerosol
309 distribution.

310

311 **2.4 Observation**

312 In this study, we focused on the aerosol chemical component of EC as the primary
313 particle and sulfate as the secondary particle. To evaluate the model results over the
314 Kanto region, we used observations of the surface mass concentrations of EC and
315 sulfate in four cities under Project FAMIKA: Maebashi/Gunma (139.10°E, 36.40°N),
316 Kisai/Saitama (139.56°E, 36.09°N), Komae/Tokyo (139.58°E, 35.64°N) and
317 Tsukuba/Ibaraki (140.12°E, 36.05°N). The EC particles in PM_{2.5} were collected every
318 six hours with quartz fiber filters and analyzed with the thermal/optical method
319 according to the IMPROVE protocol (Chow et al., 2001). The sulfate particles in PM_{2.5}
320 were also collected every six hours with Teflon filters and analyzed by ion
321 chromatography. In addition to the limited FAMIKA dataset, we utilized measurements
322 taken by the EANET (Acid Deposition Monitoring Network in East Asia;
323 <http://www.eanet.asia/index.html>) and the 4th national survey report of acid rain over
324 Japan in fiscal year 2007
325 (http://tenbou.nies.go.jp/science/institute/region/journal/JELA_3403041_2009.pdf) to
326 assess the monthly mean concentrations of sulfate and SO₂ at Japanese and Korean sites.

327 We also obtained Chinese measurements by *Zhang et al.* [2012], as part of the Chinese
328 Meteorological Administration Atmosphere Watch Network (CAWNET). To validate
329 the concentration of SO₂ for the Kanto region, we accessed monitoring stations operated
330 by Japanese and local governments.

331 In the validation of the meteorological fields simulated by NICAM-g6str and
332 NICAM-g6, we used meteorological fields (wind and temperature) reanalyzed by
333 NCEP-FNL over East Asia. In the Kanto region, we obtained measurements for the
334 meteorological parameters (temperature, relative humidity (RH) and wind) at or near
335 the 7 sites of Project FAMIKA and additional cities: Tsuchiura/Ibaraki (140.20°E,
336 36.07°N), which is the city nearest to Tsukuba; Yokohama/Kanagawa (139.64°E,
337 35.45°N); Chiba/Chiba (140.12°E, 35.62°N); Adachi/Tokyo (139.82°E, 35.77°N); and
338 Machida/Tokyo (139.43°E, 35.53°N), which is the city nearest to Komae, as shown in
339 Figure 1(b). For precipitation, we used a measurement taken by the Automated
340 Meteorological Data Acquisition System (AMeDAS) at 21 sites over Japan including
341 the following 10 Kanto's sites: Yokohama; Chiba; Tsukuba; Tokyo, which is near
342 Adachi; Maebashi; Huchu, which is near Machida; Konosu, which is near Kisai; Abiko
343 (140.11°E, 35.60°N); Saitama (139.59°E, 35.88°N); and Nerima (139.59°E, 35.74°N)
344 (Figure 1). To evaluate the spatial patterns of the precipitation obtained by
345 NICAM-g6str and NICAM-g6, we used the quantities of the monthly mean
346 precipitation around Japan that were derived from the Global Satellite Mapping of
347 Precipitation (GSMaP; Okamoto et al., 2005; Kubota et al., 2007; Aonashi et al., 2009;

348 Ushio et al., 2009) and the Meso Scale Model (MSM) developed by the JMA for rain
349 forecast (Saito et al., 2006). The results by MSM are generally higher accurate than
350 those in GSMaP, although the covering area in MSM is limited around Japan.

351 To evaluate the quantities of the total aerosol amounts, such as PM_{2.5}, we compared the
352 simulated PM_{2.5} concentrations with the observations at the 18 sites including the
353 FAMIKA sites and other monitoring stations operated by the Japanese and local
354 governments (Figure 1). The PM_{2.5} concentrations were continuously observed using
355 tapered element oscillating microbalance (TEOM) with Series 1400a Ambient
356 Particulate Monitor. The instruments are controlled under the temperature of 50 °C, to
357 minimize the influence of change in the ambient temperature and RH. However, it
358 includes large uncertain due to the difficulty in completely eliminate the water content
359 attached to aerosols and lacks of the calibration of the instrument in some of sites.
360 Nevertheless, the observed PM_{2.5} concentrations with hourly time resolution were still
361 useful to validate the model results.

362 In Tsukuba and Chiba, light detection and ranging (LIDAR) measurements operated by
363 the National Institute for Environmental Studies (NIES) of Japan were also available
364 (Sugimoto et al., 2003; Shimizu et al., 2004). The LIDAR unit measured vertical
365 profiles of the backscattering intensity at 532 and 1064 nm and the depolarization ratio
366 at 532 nm. The backscattering intensity was converted to the extinction coefficient, and
367 the depolarization ratio distinguished the extinction between spherical and non-spherical
368 particles. In this study, we only used vertical profiles of the extinction for spherical

369 particles. A detailed algorithm was provided by Sugimoto et al. (2003) and Shimizu et
370 al. (2004).

371

372 **3 Validation of Stretch-NICAM-SPRINTARS**

373 **3.1 Meteorological fields**

374 So far, the stretched-grid system was mainly applied to the simulations of tropical
375 cyclones or tropical convective clouds with small domain over oceans for the short-term
376 period (less than several days) (e.g., Satoh et al., 2010; Arakane et al., 2013). In this
377 study, we focused on the air pollution around Japan (for the longer period). Therefore,
378 we first focused on the general circulation of the basic meteorological fields over the
379 large domain, which can affect the air pollution over Japan. Figure 3 shows temperature
380 and winds near the surface and the model height of approximately 5 km for the model
381 bottom of MSL over Asia region (100°E-170°E, 10°N-50°N). In August, North Pacific
382 High (or Ogasawara High) mainly brings clear weather around Japan. A frequency of
383 the precipitation is usually limited, but a total amount of the monthly mean precipitation
384 is not small, because of typhoons and shower rain. In the focusing region, the general
385 meteorological fields simulated by NICAM-g6str and NICAM-g6 are comparable to
386 those obtained by NCEP-FNL. The absolute biases in the temperature between
387 NICAM-g6str and NCEP-FNL or between NICAM-g6 and NCEP-FNL are within
388 1.5 °C. At the model height of 5 km, the NICAM-g6str-simulated temperature tends to
389 be larger than NICAM-g6-simulated one by at most 3 °C, probably because the spatial

390 resolution in NICAM-g6str is finer than that in NCEP-FNL. These positive biases
391 between NICAM-g6str and NCEP-FNL can be seen around Japan. As for wind, western
392 winds over the northeastern part of Japan in both NICAM-g6str and NICAM-g6 are
393 stronger compared to those in NCEP-FNL. With the exception of this bias, the
394 performances of both NICAM-g6str and NICAM-g6 are good. Therefore, it is
395 concluded that the general circulations obtained by the stretched as well as the
396 uniformed grid systems are well reproduced under the nudging technique in this study.

397 To evaluate the model performances of the six-hourly instant concentrations of aerosol
398 chemical species and SO₂ over the main target region, i.e., Kanto area, we used the
399 six-hourly instant observations of temperature, RH, wind and precipitation at each
400 station over the Kanto area shown in Figure 1. The results and summary are shown in
401 Figures 4 to 7 and Table 1. The NICAM-g6 results, especially in terms of diurnal
402 variations, tend to be far from the observations compared to the NICAM-g6str results,
403 because NICAM-g6, with the horizontal resolution of approximately 100 km, does not
404 fully resolve the topology over the Kanto area. Figure 4 illustrates the temporal
405 variations of temperature at a height of 2 m. The temporal variations in the
406 NICAM-g6-simulated temperature are generally comparable to those in the observed
407 temperatures with root-mean-square-error (RMSE) values of less than 3°C, with the
408 exception of the results obtained for Maebashi and Machida. At these two sites, the
409 mean values of the NICAM-g6str-simulated temperatures are lower than those of the
410 observed temperatures by a maximum of 3.6°C. The correlation coefficients (R)

411 between NICAM-g6str and the observation range from 0.7–0.9, whereas the R between
412 NICAM-g6 and the observation range from 0.7–0.8, as shown in Table 1. Figure 5
413 shows the temporal variations in RH at a height of 2 m. The temporal variations in the
414 NICAM-g6str-simulated RH are similar to the observations, with the RMSEs in the
415 range of 10–15%. In contrast, the NICAM-g6-simulated RH is overestimated compared
416 to the observations, with the RMSEs in the range of 16–26%. The R values of RH
417 between the simulation (both NICAM-g6str and NICAM-g6) and observations are
418 approximately 0.6–0.8 (Table 1).

419 The temporal variations in the wind direction and speed simulated by NICAM-g6str are
420 compared with the observations in Figures 6 and 7. Near the southern part of the Kanto
421 area (Yokohama, Tsuchiura, Adachi and Machida), with the exception of Chiba, the
422 NICAM-g6str-simulated wind direction is generally comparable to the observations,
423 with a slight overestimation of the both NICAM-g6str and NICAM-g6 simulated wind
424 speed compared with the observations. At these four sites, the R and RMSE values in
425 NICAM-g6str range from approximately 0.5–0.7 and approximately 1.7–2.3 m/s,
426 respectively. In Chiba located near the ocean, the R value of wind speed between
427 NICAM-g6str and the observation is 0.41, whereas the NICAM-g6str-simulated wind
428 directions generally agree with the observations. Conversely, at Maebashi and Kisai, the
429 daily variations in the both NICAM-g6str and NICAM-g6 simulated wind directions
430 differ significantly from those in the observations, in which the southern winds and
431 northern winds frequently occur during the day and night, respectively, for example,

432 during August 5–12. At these two sites, the NICAM-g6-simulated wind direction and
433 speed is not closer to the observations compared to those obtained by NICAM-g6str.
434 The R value for wind speed between the NICAM-g6str and the observations at these
435 sites is estimated to be approximately 0.2. The observed southeasterly wind is long sea
436 breeze toward Maebashi Plateau surrounded on three sides by mountains around
437 Maebashi. The observed winds are caused by daytime meso-scale thermal lows
438 developed over the central Japan covering the Japanese Alps (Kuwagata and Sumioka,
439 1991). The Japanese Alps with the highest terrain in Japan can affect the local
440 meteorological fields even around 100-200 km away (Kitada et al., 1998). Therefore, it
441 suggests that the horizontal resolution in this study using NICAM-g6str (10 km over the
442 Kanto area) does not fully resolve the complex terrains of the Japanese Alps and the
443 Maebashi plateau. Therefore, it suggests that it is inadequate to simulate the wind
444 patterns and the diurnal transitions near high mountains around the Kanto area, whereas
445 it is adequate to simulate them around the center of the Kanto area.

446 Figures 8-10 show comparisons of NICAM-g6str and NICAM-g6 simulated
447 precipitation with the observations. Figure 8 compares the simulated precipitation with
448 the MSM and GSMaP derived results. During the early August 2007, mainly due to
449 passing of a typhoon over the western Japan, Okinawa, and Korea, the August mean
450 precipitation in the western Japan is larger than that in the eastern Japan, especially the
451 Kanto area. The monthly mean precipitation is estimated to be more than 200
452 mm/month over the western Japan, whereas that is estimated to be less than 50

453 mm/month over the eastern Japan. The horizontal patterns of the precipitation obtained
454 by NICAM-g6str in East China Sea, Sea of Japan near the Japan coast, and Korea are
455 closer to those derived from MSM and GSMaP than those obtained by NICAM-g6. In
456 the Kanto area, however, the NICAM-g6str-simulated precipitation with the range of
457 50-200 mm/month is overestimated compared to the MSM and GSMaP results. The
458 NICAM-g6-simulated precipitation over the Kanto area with the range of 100-200
459 mm/month is also much overestimated. In Figure 9 showing the temporal variations in
460 the amount of precipitation per day at 21 Japanese sites, the observed precipitation is
461 extremely limited during August 7-19 in the Kanto area. In other regions, the magnitude
462 of the precipitation is strong, although the precipitation is sporadic. In terms of the
463 frequency of the precipitation, the NICAM-g6str performance is better than the
464 NICAM-g6 one. Figure 10 illustrates the predictive value of daily precipitation, defined
465 as the ratio of the number of days where the model correctly predicts the weather (less
466 than 1 mm/day or more than 1 mm/day) to the number of the whole days. In the
467 NICAM-g6str results, the predictive values at most of sites over the Kanto area and four
468 sites over the non-Kanto area such as Nagoya and Osaka are calculated to be more than
469 85%. The predictive values obtained by NICAM-g6-str are mostly higher than those
470 obtained by NICAM-g6. During the rainy days such as August 20, 22 and 23 over the
471 Kanto area, both NICAM-g6str and NICAM-g6 capture the precipitation, whereas
472 NICAM-g6str reproduces greater amounts of the precipitation and NICAM-g6
473 reproduces longer periods and larger areas compared to the observations. NICAM-g6str
474 does not always capture a sudden shower, as general meteorological models have

475 difficulties in predicting this type of precipitation system (e.g., Kawabata et al., 2011).
476 To increase the accuracy of such precipitation, more sophisticated cloud-microphysics
477 model, e.g., NICAM-NDW6 model proposed by Seiki and Nakajima (2014) based on
478 the double-moment bulk scheme with six water categories, may be required. In the
479 western Japan, during the rainy days, e.g., August 22-23, both NICAM-g6str and
480 NICAM-g6 usually capture large-scaled precipitation (Figure 9). Overall, NICAM-g6str
481 usually reproduces the observed weather in the target regions and periods with a large
482 uncertainty, whereas NICAM-g6 does not capture general feature such as the sporadic
483 precipitation.

484

485 **3.2 Aerosol fields**

486 **3.2.1 Evaluation of chemical species**

487 Figures 11, 12, and 13 illustrates the temporal variations in the surface EC, sulfate, and
488 SO₂ concentrations at the four stations (Maebashi, Kisai, Komae and Tsukuba) in the
489 Kanto area using the simulations and the measurements. The simulations include
490 NICAM-g6str, NICAM-g6, and the Community Multiscale Air Quality (CMAQ) driven
491 by the Weather Research and Forecasting (WRF) model named WRF-CMAQ shown by
492 their Figures 5 and 6 of Shimadera et al. (2013). Shimadera et al. (2013) calculated the
493 WRF-CMAQ with a horizontal resolution of 5 km and an emission inventory that is
494 similar to that in the present study. Table 2 summarizes the statistical parameters for the
495 concentrations of EC, sulfate, and SO₂. The temporal variation and the average of EC

496 simulated by NICAM-g6str are better agreement with the observations obtained for
497 Komae than those simulated by NICAM-g6 (Figure 11(c)). However, the averages of
498 both NICAM-g6str and NICAM-g6 simulated EC concentrations at the other sites are
499 much underestimated compared to the observations (Table 2). For Tsukuba shown in
500 Figure 11(d), both the NICAM-g6str and NICAM-g6 simulated EC concentrations tend
501 to be underestimated compared with the observed concentrations, especially during the
502 daytime, even though the temporal variation of EC obtained by NICAM-g6str is closer
503 to the observed one compared to those obtained by NICAM-g6. At Maebashi and Kisai,
504 the temporal variation and the averages of EC obtained by NICAM-g6 are also
505 underestimated compared with the observations by a factor of three to five.
506 NICAM-g6str tends to have daily maximums of EC concentrations during the morning
507 time, whereas NICAM-g6 tends to have daily maximums during the nighttime. The
508 temporal variations of NICAM-g6str-simulated EC concentrations are generally
509 comparable to those by WRF-CMAQ shown in Figure 11 and their Figure 3 of Chatani
510 et al. (2014), with the exception of the results at Maebashi and Kisai where the EC
511 concentrations obtained by NICAM-g6str are smaller than those obtained by
512 WRF-CMAQ. At these sites, the difference in the EC concentrations between
513 NICAM-g6str and WRF-CMAQ is probably caused by the difference in the horizontal
514 resolution, which is most likely critical for properly simulating the air pollution
515 delivered by the meteorological wind fields from the center of the Kanto region (Kusaka
516 and Hayami, 2006). Table 2 also shows that the R obtained by NICAM-g6str at all sites
517 are high or moderate, with the exception of Maebashi, whereas those obtained by

518 NICAM-g6 and CMAQ are low. At most sites, the EC concentrations obtained by
519 WRF-CMAQ shown in Figure 11, and WRF-CMAQ illustrated by Morino et al.
520 (2010a,b) and Chatani et al. (2014), NICAM-g6str, and NICAM-g6 are also
521 underestimated compared to the observations with the larger values of RSME. The
522 underestimation of EC concentrations is investigated by sensitivity tests of EC emission
523 inventory in section 3.2.2.

524 At the same four sites, simulated sulfur components (sulfate and SO₂) are compared
525 with the observations in Figures 12 and 13. The observed SO₂ represents the ensemble
526 results of monitoring stations operated by Japanese and local governments around each
527 FAMIKA site. The mean differences in the sulfate mass concentrations between
528 NICAM-g6str and the observations are within approximately 10% at Maebashi and
529 Tsukuba, approximately -30% at Komae, and approximately +40% at Kisai. At all sites,
530 the temporal variations of the NICAM-g6str-simulated sulfate concentrations are
531 generally comparable to those obtained by the observations and WRF-CMAQ shown in
532 Figure 12 (i.e., their Figure 6 of Shimadera et al., 2013) and illustrated in their Figure 3
533 of Morino et al. (2010a), whereas the differences in the sulfate concentrations between
534 NICAM-g6str and the observations are somewhat greater on August 7 and 8 at
535 Maebashi where the performance of NICAM-g6str is relatively poor, mainly due to the
536 inadequate horizontal resolution to reproduce the observed meteorological fields, as
537 shown in section 3.1. The use of the prescribed distributions of three hourly averaged
538 monthly oxidants may partly cause the discrepancy of the hourly variations of the

539 sulfate between NICAM-g6str and the observations. The R obtained by all the models
540 (NICAM-g6str, NICAM-g6, and WRF-CMAQ) is acceptable at most sites, with the
541 exception of NICAM-g6str at Maebashi and WRF-CMAQ at Kisai. The RMSEs
542 obtained by all the models are smaller at Komae and Tsukuba than those at Maebashi
543 and Kisai. The six-hourly variations of the sulfate obtained by WRF-CMAQ are
544 sometimes missed by NICAM-g6str, partly due to the use of the prescribed oxidants.
545 Even though NICAM-g6 reproduces the weekly cycle of the observed sulfate, it has
546 difficulties in simulating the diurnal cycle of the observed and NICAM-g6str-simulated
547 sulfate, as shown in the results of EC by Figure 11. The averages of the sulfate
548 concentrations obtained by NICAM-g6 tend to be smaller than those by NICAM-g6str
549 and the observations. The possible impacts of the prescribed oxidant on the sulfate
550 concentrations are investigated in section 3.2.2.

551 In Figure 13, NICAM-g6str and NICAM-g6 simulated SO₂ concentrations are
552 compared by the observations. In the previous studies, the comparison in SO₂
553 concentrations between the simulation and observation was very limited, with the
554 exception of their Figure 4 of Morino et al. (2010b), which showed large differences in
555 the SO₂ concentrations between WRF-CMAQ and the observations by more than a
556 factor of two. The R between NICAM-g6str and the observations are low, with the
557 exception of Komae (R=0.62), but are approximately within the range obtained by
558 WRF-CMAQ in Morino et al. (2010b). The differences in the mean SO₂ concentrations
559 between NICAM-g6str and the observations and between NICAM-g6 and the

560 observations are within approximately 20% at all sites, with the exception of
561 NICAM-g6str at Maebashi and NICAM-g6str at Tsukuba (Table 2). The temporal
562 variations in the simulated SO₂ concur with those in the observations. The observations
563 sometimes show high SO₂ concentrations at all sites, e.g., up to 20 ppbv at Komae, in
564 the afternoon on August 12 and 14. On August 12, NICAM-g6str normally reproduced
565 the peaks of the observed SO₂, but with the blunter and slightly shifted peaks. On
566 August 14, both NICAM-g6str and NICAM-g6 did not reproduce the sharp peaks of the
567 observed SO₂, especially at Komae and Tsukuba. It may imply that special
568 meteorological fields cause the observed peaks on August 12, whereas local SO₂
569 emission is stronger on August 14. The latter issue is improved by processing
570 time-highly-resolved emission inventories of SO₂, which can be estimated through a
571 top-down approach using a data assimilation (Schutgens et al., 2012; Xu et al., 2013).

572 To assess the performance of both NICAM-g6str and NICAM-g6 in simulating the
573 distributions of the air pollutants over Japan, we compared the August averages of the
574 simulated EC, sulfate and SO₂ concentrations with the available measurements (Figures
575 14 and 15). Although the EC observatories are limited, both the NICAM-g6str and
576 NICAM-g6 simulated EC concentrations are much underestimated compared to the
577 observations, with the relative bias (*Br*), defined as a ratio of the simulated value to the
578 observed one, to be 0.15 (NICAM-g6str) and 0.16 (NICAM-g6). In China, the
579 NICAM-g6str-simulated EC concentrations are comparable to the
580 NICAM-g6-simulated ones with the R values of 0.71 (NICAM-g6str) and 0.68

581 (NICAM-g6), whereas at the Japanese urban areas such as Nagoya (136.97°E, 35.17°N)
582 and Osaka (135.54°E, 34.68°N), the NICAM-g6str-simulated EC concentrations are
583 larger than NICAM-g6-simulated ones.

584 The NICAM-g6str-simulated sulfate concentrations are larger and more comparable to
585 the observations over China compared to NICAM-g6-simulated ones. In Japan, the hot
586 spots with greater concentrations of more than $5 \mu\text{g}/\text{m}^3$ are found only in the
587 NICAM-g6str results. The *Br* values are estimated to be 0.59 (NICAM-g6str) and 0.53
588 (NICAM-g6), whereas the *R* values are estimated to be 0.78 (NICAM-g6str) and 0.88
589 (NICAM-g6), respectively. The results indicate that the sulfate concentrations obtained
590 by both NICAM-g6str and NICAM-g6 tend to be underestimated by approximately
591 40-50% compared with the observed sulfate concentrations. The underestimation is
592 mainly caused by the underestimation in China and possibly by the uncertainty of the
593 simulated precipitation around Japan. At Hedo located at Okinawa islands, for example,
594 the underestimation of both NICAM-g6str and NICAM-g6 simulated sulfate
595 concentrations is caused by a possible underestimation of transboundary sulfate from
596 the continent, which is attributed to a large uncertainty of the precipitation fields
597 modulated by typhoon in the early August. However, the correlations between the
598 simulations and observations are adequately acceptable. It suggests that the use of the
599 prescribed oxidants for sulfate formation is not crucial for predicting monthly averaged
600 sulfate mass concentrations at least if the diurnal and seasonal variations of the
601 prescribed oxidants are considered. The simulated and observed SO_2 concentrations also

602 correlate, with the R value of 0.63 (NICAM-g6str) and 0.48 (NICAM-g6). The Br
603 values are calculated to be 0.48 (NICAM-g6str) and 0.67 (NICAM-g6). Figure 15
604 shows that the SO₂, which is a primary product, is localized near the source areas,
605 whereas sulfate, which is as a secondary product, is distributed from the source to the
606 outflow areas. Although EC is also a primary product, the horizontal distributions of
607 NICAM-g6str-simulated EC are smaller than those of NICAM-g6str-simulated SO₂,
608 possibly because SO₂ near the surface is more scavenged through the dry deposition
609 process compared to EC.

610

611 **3.2.2 Uncertainty in the simulation**

612 Sensitivity tests were conducted to examine potential uncertainties derived from
613 prescribed datasets related to EC and sulfate for the NICAM-g6str simulations. For the
614 EC sensitivity tests, the emission quantities were set to half and twice of those used in
615 the standard run in this study. The results for the FAMIKA sites are shown in Figure
616 16(a) in which the bars show the simulated EC concentrations for both sensitivity tests.
617 For the majority of the sites, with the exception of Komae, the results obtained by the
618 sensitivity experiments of twice strength remain underestimated compared with the
619 measurements. The large underestimation of the EC mass concentrations at Maebashi
620 and Kisai was also shown by WRF-CMAQ of Shimadera et al. (2013) as well as the
621 previous studies of WRF-CMAQ in Morino et al. (2010a,b) and Chatani et al. (2014).
622 However, Fushimi et al. (2011) and Chatani et al. (2014) suggested that the difference

623 in the EC concentrations between WRF-CMAQ and the measurements is largely
624 attributed to an underestimation of the EC emission inventory, especially open biomass
625 burning from domestic sources. The local EC emission can be estimated by a
626 combination of the data assimilation and intensive measurements (Schutgens et al.,
627 2012; Wang et al., 2012; Yumimoto and Takemura, 2013).

628 Sensitivity experiments of the SO₂ emissions and the prescribed OH radical used in
629 sulfur chemistry were executed under half and twice the amounts used in the standard
630 experiment. The results for the FAMIKA sites are shown in Figure 16(b) in which the
631 bars show the simulated sulfate concentrations for both sensitivity tests under the
632 different experiments. Compared with the SO₂ emissions used in the standard
633 experiment, the doubled amount of SO₂ emissions can overcome the slight
634 underestimation of the simulated sulfate compared with the observations. Therefore, the
635 emission inventories of SO₂ should be improved for the better simulation of the sulfate.

636 In this sensitivity tests for oxidants, the SO₂ oxidation by OH radical strongly depends
637 on the OH concentrations as well as the cloud cover area, whereas the SO₂ oxidation by
638 ozone and hydrogen peroxide mainly depends on their concentrations, the cloud cover
639 area, and the cloud water content. The cloud distributions are modulated by some
640 feedbacks of the sulfate formation through the aerosol direct and indirect effects. As a
641 result, the sensitivity of the OH radical concentrations to the simulated sulfate
642 concentration is smaller than that we expected and that to the SO₂ emissions. We also
643 determined that the sensitivities of the other oxidants to the simulated sulfate

644 concentrations were small (not shown). These results also suggest that the use of the
645 prescribed oxidants for sulfate formation is not crucial for predicting weekly-averaged
646 sulfate mass concentrations at least by taking into account for diurnal and seasonal
647 variations of the prescribed oxidants. At the same time, they also suggest that the
648 relationship between the oxidants and the sulfate concentrations through the feedbacks
649 is non-linear and complex, and thus the sensitivity of the oxidants to the simulated
650 sulfate should be investigated.

651

652 **3.2.3 PM2.5**

653 Figure 17 shows the temporal variation in the surface PM2.5 mass concentration at the
654 18 Japanese sites including 10 sites in the Kanto area. At most of the sites, both
655 NICAM-g6str and NICAM-g6 usually captures the weekly variation of the observed
656 PM2.5, whereas only NICAM-g6str reproduces the diurnal variation of the observed
657 PM2.5. Table 3 shows the PM2.5 concentrations in daily, daytime (from 9 am to 4 pm),
658 and nighttime (from 9 pm to 4 am) averages and ratios of daytime to nighttime. The
659 results show that the simulated PM2.5 concentrations are underestimated compared with
660 the observations by more than a factor of two and by up to four at Maebashi. In addition,
661 the results show that the NICAM-g6str-simulated ratios (0.9-1.3) are larger than
662 NICAM-g6-simulated ones (0.8-0.9), whereas the NICAM-g6str-simulated ones are
663 smaller than the observed values (1.0-1.8). At Maebashi, where the ratio is higher than
664 that at other sites, the issue of the poor model performance of the meteorological fields

665 can be a major reason of the large underestimation, as mentioned in section 3.1. At all
666 sites, the possible underestimation of SOA may be a critical issue, as shown in the fact
667 that the clear diurnal variation of PM_{2.5} during August 4-9 and suggested by previous
668 studies (Matsui et al., 2009; Morino et al., 2010c). Morino et al. (2010c) implied that
669 over the Kanto area SOA from anthropogenic sources, which were disregarded in this
670 study, are large portion of total carbonaceous aerosols, even though WRF-CMAQ does
671 not correctly reproduce such carbonaceous aerosols. More sophisticated SOA module,
672 e.g., volatility basis-set approach proposed by Donahue et al. (2006) based on the
673 categorization of organic vapors with similar volatility, is required for to produce SOA
674 with higher accuracy. Originally, the underestimation of PM_{2.5} is common among
675 previous studies that employed regional aerosol-transport models (Morino et al., 2010b,
676 Chatani et al., 2011), primarily because the concentrations of the observed PM_{2.5}
677 include undefined chemical species with mean fractions ranging from approximately
678 30–50% in the total PM_{2.5} in the summer of Japan (datasets from the Tokyo
679 Environment Agency and the Kawasaki Municipal Research Institute for Environmental
680 Protection). Another possible reason is that the PM_{2.5} mass concentration includes
681 water attached to aerosols, depending on the ambient RH conditions. Therefore, these
682 undefined chemical compounds in this study may account for a large portion of the
683 difference between the simulated and the observed values.

684 To evaluate the vertical profiles of the PM_{2.5} mass concentrations, we used the LIDAR
685 observation operated by the NIES-Japan network. Figure 18 shows the average results

686 for the simulated and observed extinction coefficient of the spherical particles at
687 Tsukuba and Chiba in August. At both sites, the vertical profiles and the magnitudes
688 below 3 km height of the simulated extinction by both NICAM-g6str and NICAM-g6
689 are comparable to the observed results, whereas the simulated extinction values tend to
690 be smaller than the observed extinction values near the surface. These results near the
691 surface are consistent with those obtained by the surface PM2.5 comparison shown in
692 Figure 17. In contrast, the extinction values observed by LIDAR include large
693 variabilities, primarily because they are retrieved from the surface to the cloud base,
694 which highly varies hour-by-hour and is basically difficult to detect with the high
695 accuracy, and secondly because they depend not only on the PM2.5 mass concentrations
696 but also on the ambient RH and the water amount attached to aerosols. At both sites, the
697 differences in the extinction between NICAM-g6str and NICAM-g6 are small below 1
698 km height, whereas those are relatively large above 1 km height. The differences are
699 attributed to the differences in the primary particles, mainly carbonaceous aerosols,
700 between NICAM-g6str and NICAM-g6 (not shown). It means that it is attributed to the
701 difference in the vertical transport between different spatial resolutions. Therefore,
702 impacts of the difference in the spatial resolution on the distributions of both aerosols
703 and their precursors should be addressed in the future work.

704

705 **4 Summary**

706 An aerosol-coupled global nonhydrostatic model, which is based on the aerosol module
707 of Spectral Radiation-Transport Model for Aerosol Species (SPRINTARS) and the
708 global cloud-resolving model of Nonhydrostatic Icosahedral Atmospheric Model
709 (NICAM), with a horizontal resolution of approximately 10 km or less in the target
710 region, is proposed in the present study. Circulations over both the global and target
711 domains are solved with a single model, whose mesh size varies with fine meshes
712 covering the target region, to calculate meso-scale circulations in the study region. The
713 stretched global model requires lower computational costs to simulate atmospheric
714 aerosols with fine horizontal resolutions compared with the global uniform
715 nonhydrostatic model, whereas it may require higher computational costs compared
716 with the general regional models, because the stretched-grid system calculates inside
717 and outside the target domain. As opposed to the general regional models, the
718 stretched-grid system does require neither nesting techniques nor boundary conditions.

719 In this study, we developed the new-type regional model with a horizontal resolution of
720 approximately 10 km to simulate aerosols over Japan, especially in the megacities of the
721 Kanto area, including Tokyo. To evaluate the model performances in the stretched-grid
722 system (hereafter referred to as the “NICAM-g6str”), we also simulated
723 NICAM-SPRINTARS with the globally uniformed grid simulation in glevel-6
724 resolution (the horizontal resolution is set to 110 km and we call it “NICAM-g6”). Both
725 NICAM-g6str and NICAM-g6 well reproduce general circulations obtained by
726 reanalysis of NCEP-FNL under the nudging technique over Asia including the target

727 region. Only NICAM-g6str usually reproduces both diurnal and weekly variations of
728 the observed weather (temperature, wind, and precipitation) around Japan. Both
729 NICAM-g6str and NICAM-g6 generally reproduce monthly mean distributions of the
730 observed sulfate and SO₂ over East Asia, with the high correlations of more than 0.5,
731 but the underestimation of the simulated concentrations by 40% (NICAM-g6str) and
732 50% (NICAM-g6). The underestimation is mainly caused by the underestimation in
733 China and possibly by the uncertainty of the simulated precipitation around Japan. In
734 the Kanto area, the results obtained by NICAM-g6str are much closer to the
735 observations compared to those obtained by NICAM-g6. Only NICAM-g6str succeeds
736 in simulating the wind patterns and the diurnal transitions around the center of the
737 Kanto area, although it is inadequate to simulate the wind patterns and the diurnal
738 transitions at some sites located at the edge of the Kanto area and surrounded on three
739 sides by mountains, e.g., Maebashi, mainly due to the insufficient horizontal resolution.
740 NICAM-g6str also generally reproduces both diurnal and weekly variations of the
741 observed and/or a regional aerosol-transport model (WRF-CMAQ) simulated EC,
742 sulfate, and SO₂ concentrations, especially with their high correlation ($R > 0.5$) at
743 Komae/Tokyo. The standard and sensitivity experiments suggest that (1) emission
744 inventories of EC and SO₂ should be improved for the better simulation and (2) the use
745 of the prescribed oxidants for the sulfate formation is not crucial for predicting weekly
746 and monthly averaged sulfate mass concentrations at least if the diurnal and seasonal
747 variations of the prescribed oxidants are considered. As for PM_{2.5} simulations, only
748 NICAM-g6str captures both weekly and diurnal cycles of PM_{2.5}, with the exception of

749 the underestimation of the simulated PM_{2.5} by at least twice, probably due to the
750 underestimation of secondary organic aerosol (SOA) from anthropogenic sources and
751 the high uncertainties of the measurements.

752 Therefore, this new seamless aerosol-transport model, which covers global to regional
753 scales, can be applied to regional simulations. It suggests that even the simplified
754 aerosol module (e.g., prescribed oxidants for sulfur chemistry) is applicable for the
755 regional simulation if the module is coupled to a dynamic core with high horizontal
756 resolution. To more accurately simulate areas around Japan and develop the simplified
757 aerosol module, we need to address the following objectives: (1) to increase the
758 horizontal resolution (less than 10 km) to properly resolve wind fields, which can
759 greatly influence the delivery of air pollution from Tokyo to subcities such as
760 Maebashi; (2) to accurately reproduce the cloud and precipitation fields caused by
761 thermal lows, for example, by applying the finer horizontal resolution and/or more
762 sophisticated schemes of cloud microphysics such as the double-moment bulk scheme
763 proposed by Seiki and Nakajima (2014); (3) to use better emission inventories by
764 developing a data assimilation such as the Kalman smoother proposed by Schutgens et
765 al. (2012) with intensive measurements in many sites; (4) to simulate strong peaks of
766 PM_{2.5} in the daytime in the Kanto region by implementing more sophisticated module
767 of SOA formed from both anthropogenic and biogenic sources, such as the volatility
768 basis-set approach proposed by Donahue et al. (2006), in this model; and (5) to treat
769 nitrate aerosol through a thermodynamic equilibrium in the simulation of wintertime

770 and/or future scenarios where the relative contribution of nitrate will be larger than that
771 of sulfate under the changes in emission of NO_x and SO₂ (e.g., Ohara et al., 2007).
772 These issues are directly connected to the further development of NICAM-SPRINTARS
773 in both regional and global simulations. Near the future, we will present scenario
774 experiments at regional scales of 10 km grids and/or address the issue of regional air
775 quality and its health impacts in densely populated megacities.

776

777 **Acknowledgements**

778 We acknowledge the developers of NICAM and SPRINTARS, especially K. Suzuki
779 and T. Takemura, and the researchers from FAMIKA, especially S. Hasegawa and Y.
780 Morino, and Y. R. Li and A. Miyaji for their assistance with processing the datasets. We
781 are grateful to the GTOPO30 courtesy of the U.S. Geological Survey, the NCEP-FNL,
782 EAGrid2000 by A. Kannari, and the local government measurements provided by the
783 Tokyo Environment Agency, the Gunma Prefectural Institute of Public Health and
784 Environmental Sciences and the Kawasaki Municipal Research Institute for
785 Environmental Protection. We are also grateful to the working group members of
786 Project SALSA and the Ministry of Education, Culture, Sports and Science and
787 Technology (MEXT). Some of the authors were supported by Project SALSA, which is
788 part of the Research Program on Climate Change Adaptation (RECCA) by the MEXT
789 in Japan, the Global Environment Research Fund S-12 and A-1101 of the Ministry of
790 the Environment (MOE) in Japan, MOE/GOSAT, JST/CREST/EMS/TEEDDA,
791 JAXA/EarthCARE, GCOM-C, MEXT/VL for climate diagnostics and

792 MEXT/KAKENHI/Innovative Areas 2409. The model simulations were performed
793 using supercomputer resources, SR16000 and PRIMEHPC FX10 from the University of
794 Tokyo, Japan.
795

796 **References**

- 797 Aonashi, K., Awaka, J., Hirose, M., Kozu, T., Kubota, T., Liu, G., Shige, S., Kida, S.
798 Seto, S., Takahashi, N., and Takayabu, Y. N.: GSMaP passive, microwave
799 precipitation retrieval algorithm: Algorithm description and validation. *J. Meteor.*
800 *Soc. Japan*, 87A, 119-136, 2009.
- 801 Arakane, S., Satoh, M., and Yanase, W.: Excitation of deep convection to the north of
802 tropical storm Bebinca (2006), *J. Meteorol. Soc. Japan*, 92(2), 141-161,
803 doi:10.2151/jmsj.2014-201, 2014.
- 804 Arakawa, A., and Schubert, W. H.: Interactions of cumulus cloud ensemble with the
805 large-scale environment, part I, *J. Atmos. Sci.*, 31, 674–701, doi:
806 10.1175/1520-0469(1974)031<0674:IOACCE>2.0.CO;2, 1974.
- 807 Barrie, L. A., Yi, Y., Leitch, W. R., Lohmann, U., Kasibhatla, P., Roelofs, G.-J.,
808 Wilson, J., McGovern, F., Benkovitz, C., Melieres, M. A., Law, K., Prospero, J.,
809 Kritz, M., Bergmann, D., Bridgeman, C., Chin, M., Christensen, J., Easter, R.,
810 Feichter, J., Land, C., Jeuken, A., Kjellstrom, E., Koch, D., and Rasch, P.: A
811 comparison of large-scale atmospheric sulphate aerosol models (COSAM):
812 overview and highlights, *Tellus*, 53B, 615-645, 2001.
- 813 Berry, E. X.: Cloud droplet growth by collection, *J. Atmos. Sci.*, 24, 688-701, 1967.
- 814 Carmichael, G. R., Adhikari, B., Kulkarni, S., D’Allura, A., Tang, Y., Streets, D.,
815 Zhang, Q., Bond, T. C., Ramanathan, V., Jamroensan, A., and Marrapu, P.: Asian
816 Aerosols: Current and year 2030 distributions and implications to human health and
817 regional climate change, *Environ. Sci. Technol.*, 43, 5811-5817,

818 doi:10.1021/es8036803, 2009.

819 Chatani, S., Morikawa, T., Nakatsuka, S., and Matsunaga, S.: Sensitivity analysis of
820 domestic emission sources and transboundary transport on PM_{2.5} concentrations in
821 three major Japanese urban areas for the year 2005 with the three-dimensional air
822 quality simulation, *J. Jpn. Soc. Atmos. Environ.*, 46, 101-110, 2011 (in Japanese).

823 Chatani, S., Morino, Y., Shimadera, H., Hayami, H., Mori, Y., Sasaki, K., Kajino, M.,
824 Yokoi, T., Morikawa, T., and Ohara, T.: Multi-model analyses of dominant factors
825 influencing elemental carbon in Tokyo metropolitan area of Japan, *Aerosol and Air
826 Quality Research*, 14, 396-405, 2014.

827 Chow, J. C., Watson, J. G., Crow, D., Lowenthal, D. H., and Merrifield, T.: Comparison
828 of IMPROVE and NIOSH carbon measurements. *Aerosol Sci. Technol.*, 34, 23–34,
829 2001.

830 Chung, J. Y., Honda, Y., Hong, Y. -C., Pan, X. -C., Guo, Y. -L., and Kim, H.: Ambient
831 temperature and mortality: An international study in four capital cities of East Asia,
832 *Sci. Total Environ.*, 408, 390-396, doi:10.1016/j.scitotenv.2009.09.009, 2009.

833 Dai, T., Goto, D., Schutgens, N.A.J., Dong, X., Shi, G., and Nakajima, T.: Simulated
834 aerosol key optical properties over global scale using an aerosol transport model
835 coupled with a new type of dynamic core, *Atmos. Environ.*, 82, 71-82,
836 doi:10.1016/j.atmosenv.2013.10.018, 2014a.

837 Dai, T., Schutgens, N. A. J., Goto, D., Shi, G., and Nakajima, T.: Improvement of
838 aerosol optical properties modeling over Eastern Asia with MODIS AOD
839 assimilation in a global non-hydrostatic icosahedral aerosol transport model,

840 Environmental Pollution, 195, 319-329, DOI: 10.1016/j.envpol.2014.06.021, 2014.

841 Diehl, T., Heil, A., Chin, M., Pan, X., Streets, D., Schulz, M., and Kinne, S.:

842 Anthropogenic, biomass burning, and volcano emissions of black carbon, organic

843 carbon, and SO₂ from 1980 to 2010 for hindcast model experiments, Atmos. Chem.

844 Phys. Discuss., 12, 24895-24954, doi:10.5194/acpd-12-24895-2012, 2012.

845 Dockery, D. W., Pope III, C. A., Xu, X., Spengler, J. D., Ware, J. H., Fay, M. E., Ferris,

846 Jr., B. G., and Speizer, F. E.: An association between air pollution and mortality in

847 six U.S. cities, New Engl. J. Med., 329, 1753-1759,

848 doi:10.1056/NEJM199312093292401, 1993.

849 Donahue, N. M., Robinson, A. L., Stanier, C. O., and Pandis, S. N.: Coupled

850 partitioning, dilution, and chemical aging of semivolatile organics, Environ. Sci.

851 Technol., 40, 2635-2643, 2006.

852 Forster, P., Ramaswamy, V., Artaxo, P., Berntsen, T., Betts, R., Fahey, D. W.,

853 Haywood, J., Lean, J., Lowe, D. C., Myhre, G., Nganga, J., Prinn, R., Raga, G.,

854 Schulz, M., and Van Dorland, R.: Changes in Atmospheric Constituents and in

855 Radiative Forcing. In: Climate Change 2007: The Physical Science Basis.

856 Contribution of Working Group I to the Fourth Assessment Report of the

857 Intergovernmental Panel on Climate Change, edited by: Solomon, S., Qin, D.,

858 Manning, M., Chen, Z., Marquis, M., Averyt, K. B., Tignor, M., and Miller,

859 H. L., Cambridge University Press, Cambridge, United Kingdom and New York,

860 NY, USA, 996pp., 2007.

861 Fushimi, A., Wagai, R., Uchida, M., Hasegawa, S., Takahashi, K., Kondo, M.,

862 Hirabayashi, M., Morino, Y., Shibata, Y., Ohara, T., Kobayashi, S., and Tanabe,
863 K.: Radiocarbon (^{14}C) diurnal variations in fine particles at sites downwind from
864 Tokyo, Japan in summer, *Environ. Sci. Technol.*, 45, 6784-6792,
865 doi:10.1021/es201400p, 2011.

866 Goto, D., Nakajima, T., Takemura, T., and Sudo, K.: A study of uncertainties in the
867 sulfate distribution and its radiative forcing associated with sulfur chemistry in a
868 global aerosol model, *Atmos. Chem. Phys.*, 11, 10889-10910,
869 doi:10.5194/acp-11-10889-2011, 2011a.

870 Goto, D., Schutgens, N. A. J., Nakajima, T., and Takemura, T.: Sensitivity of aerosol to
871 assumed optical properties over Asia using a global aerosol model and AERONET,
872 *Geophys. Res. Lett.*, 38, doi:10.1029/2011GL048675, 2011b.

873 Goto, D., Takemura, T., Nakajima, T., and Badarinath, K. V. S.: Global aerosol
874 model-derived black carbon concentration and single scattering albedo over Indian
875 region and its comparison with ground observations, *Atmos. Environ.*, 45,
876 3277-3285, doi:10.1016/j.atmosenv.2011.03.037, 2011c.

877 Goto, D.: Modeling of black carbon in Asia using a global-to-regional seamless
878 aerosol-transport model, *Environmental Pollution*, 195, 330-335, DOI:
879 10.1016/j.envpol.2014.06.006, 2014.

880 Hallquist, M., Wenger, J. C., Baltensperger, U., Rudich, Y., Simpson, D., Claeys, M.,
881 Dommen, J., Donahue, N. M., George, C., Goldstein, A. H., Hamilton, J. F.,
882 Herrmann, H., Hoffmann, T., Iinuma, Y., Jang, M., Jenkin, M. E., Jimenez, J. L.,
883 Kiendler-Scharr, A., Maenhaut, W., McFiggans, G., Mentel, Th. F., Monod, A.,

884 Prevot, A. S. H., Seinfeld, J. H., Surratt, J. D., Szmigielski, R., and Wildt, J.: The
885 formation, properties and im- pact of secondary organic aerosol: current and
886 emerging issues, *Atmos. Chem. Phys.*, 9, 5155–5236, doi:10.5194/acp-9-5155-
887 2009, 2009.

888 Hasegawa, S., Kobayashi, S., Ohara, T., Tanabe, K., Hayami, H., Yomemochi, S.,
889 Umezawa, N., Iijima, A. and Kumagai, K.: Fine aerosol measurement and modeling
890 in Kanto area (1), overview of measurement. Proceedings of the 49th Annual
891 Meeting of the Japan Society for Atmospheric Environment, 377, 2008 (in
892 Japanese).

893 Holloway, T., Sakurai, T., Han, Z., Ehlers, S., Spak, S.N., Horowitz, L. W., Carmichael,
894 G. R., Streets, D. G., Hozumi, Y., Ueda, H., Park, S. U., Fung, C., Kajino, M.,
895 Thongboonchoo, N., Engardt, M., Bennet, C., Hayami, H., Sartelet, K., Wang, Z.,
896 Matsuda, K., and Amann, M.: MICS-Asia II: Impact of global emissions on
897 regional aiq quality in Asia, *Atmos. Environ.*, 42, 3543-3561, 2008.

898 Kannari, A., Tonooka, Y. Baba, T., and Murano, K.: Development of multiple-species 1
899 km x 1 km resolution hourly basis emissions inventory for Japan, *Atmos. Environ.*,
900 41, 3428-3439, 2007.

901 Kawabata, T., Kuroda, T., Seko, H., and Saito, K.: A Cloud-Resolving 4DVAR
902 Assimilation Experiment for a Local Heavy Rainfall Event in the Tokyo
903 Metropolitan Area. *Mon. Wea. Rev.*, 139, 1911–1931, 2011.

904 Kinne, S., Schulz, M., Textor, C., Guibert, S., Balkanski, Y., Bauer, S. E., Berntsen, T.,
905 Boucher, O., Chin, M., Collins, W., Dentener, F., Diehl, T., Easter, R., Feichter, J.,

906 Fillmore, D., Ghan, S., Ginoux, P., Gong, S., Grini, A., Hendricks, J., Herzog, M.,
907 Horowitz, L., Isaksen, I., Iversen, T., Kirkevåg, A., Kloster, S., Koch, D.,
908 Kristjansson, J. E., Krol, M., Lauer, A., Lamarque, J. F., Lesins, G., Liu, X.,
909 Lohmann, U., Montanaro, V., Myhre, G., Penner, J. E., Pitari, G., Reddy, S., Seland,
910 O., Stier, P., Takemura, T., and Tie, X.: An AeroCom initial assessment – optical
911 properties in aerosol component modules of global models, *Atmos. Chem. Phys.*, 6,
912 1815-1834, doi:10.5194/acp-6-1815-2006, 2006.

913 Kitada, T., Okamura, K., and Tanaka, S.: Effects of topography and urbanization on
914 local winds and thermal environment in the Nohbi Plain, coastal region of central
915 Japan: A numerical analysis by mesoscale meteorological model with a k-e
916 turbulence model, *J. Applied Met.*, 37, 1026-1046, 1998.

917 Koch, D., Bond, T. C., Streets, D., and Unger, N.: Linking future aerosol radiative
918 forcing to shifts in source activities, *Geophys. Res. Lett.*, 34, L05821,
919 doi:10.1029/2006GL028360, 2007.

920 Kubota, T., Shige, S., Hashizume, H., Aonashi, K., Takahashi, N., Seto, S., Hirose, M.,
921 Takayabu, Y. N., Nakagawa, K., Iwanami, K., Ushio, T., Kachi, M., and Okamoto,
922 K.: Global Precipitation Map using Satelliteborne Microwave Radiometers by the
923 GSMaP Project: Production and Validation, *IEEE Trans. Geosci. Remote Sens.*,
924 45(7), 2259-2275, 2007.

925 Kurokawa, J., Ohara, T., Morikawa, T., Hanayama, S., Greet, J.-M., Fukui, T.,
926 Kawashima, K., and Akimoto, H.: Emissions of air pollutants and greenhouse gases
927 over Asian regions during 2000-2008: Regional emission inventory in Asia (REAS)

928 version 2, *Atmos. Chem. Phys. Discuss.*, 13, 10049-10123, 2013.

929 Kusaka, H., and Hayami, H.: Numerical simulation of local weather for a high
930 photochemical oxidant event using the WRF model, *JSME International Journal*.
931 Ser. B. Fluids and thermal engineering, 49(1), 72-77, 2006.

932 Kuwagata, T., and Sumioka, M.: The daytime PBL heating process over complex
933 terrain in central Japan under fair and calm weather conditions, Part III: Daytime
934 thermal low and nocturnal thermal high, *J. Met. Soc. Japan*, 69(1), 91-104, 1991

935 Lamarque, J.-F., Bond, T. C., Eyring, V., Granier, C., Heil, A., Klimont, Z., Lee, D.,
936 Liou, S. C., Mieville, A., Owen, B., Schultz, M. G., Shindell, D., Smith, S. J.,
937 Stehfest, E., Van Aardenne, J., Cooper, O. R., Kainuma, M., Mahowald, N.,
938 McConnell, J. R., Naik, V., Riahi, K., and van Vuuren, D. P.: Historical
939 (1850-2000) gridded anthropogenic and biomass burning emissions of reactive
940 gases and aerosols: Methodology and application, *Atmos. Chem. Phys.*, 10,
941 7017-7039, doi:10.5194/acp-10-7017-2010, 2010.

942 Le Treut, H., and Li, Z.-X.: Sensitivity of an atmospheric general circulation model to
943 prescribed SST changes: feedback effects associated with the simulation of cloud
944 optical properties, *Clim. Dynam.*, 5, 175–187, 1991.

945 Matsui, H., Koike, M., Takegawa, N., Kondo, Y., Griffin, R. J., Miyazaki, Y., Yokouchi,
946 Y., and Ohara, T.: Secondary organic aerosol formation in urban air: Temporal
947 variations and possible contributions from unidentified hydrocarbons, *J. Geophys.*
948 *Res.*, 114, D04201, doi:10.1029/2008JD010164, 2009.

949 Mellor, G. L. and Yamada, T.: A hierarchy of turbulence closure models for planetary

950 boundary layers, *J. Atmos. Sci.*, 31, 1791-1806,
951 doi:10.1175/1520-0469(1974)031<1791:AHOTCM>2.0.CO;2, 1974.

952 Miura, H., Satoh, M., Nasuno, T., Noda, A. T., and Oouchi, K.: A Madden-Julian
953 Oscillation event realistically simulated by a global cloud-resolving model, *Science*,
954 318, 1763-1765, doi:10.1126/science.1148443, 2007.

955 Morino, Y., Chatani, S., Hayami, H., Sasaki, K., Mori, Y., Morikawa, T., Ohara, T.,
956 Hasegawa, S., and Kobayashi, S.: Evaluation of ensemble approach for O₃ and
957 PM_{2.5} simulation, *Asian Journal of Atmospheric Environment*, 4, 150-156, 2010a.

958 Morino, Y., Chatani, S., Hayami, H., Sasaki, K., Mori, Y., Morikawa, T., Ohara, T.,
959 Hasegawa, S., and Kobayashi, S.: Inter-comparison of chemical transport models
960 and evaluation of model performance for O₃ and PM_{2.5} prediction – case study in
961 the Kanto Area in summer 2007, *J. Jpn. Soc. Atmos. Environ.*, 45, 212-226, 2010b
962 (in Japanese).

963 Morino, Y., Takahashi, K., Fushimi, A., Tanabe, K., Ohara, T., Hasegawa, S., Uchida,
964 M., Takami, A., Yokouchi, Y., and Kobayashi, S.: Contrasting diurnal variations in
965 fossil and nonfossil secondary organic aerosols in urban outflow, Japan, *Environ.*
966 *Sci. Technol.*, 44, 8581-8586, 2010c.

967 Moss, R. H., Edmonds, J. A., Hibbard, K. A., Manning, M. R., Rose, S. K., van Vuuren,
968 D. P., Carter, T. R., Emori, S., Kainuma, M., Kram, T., Meehl, G. A., Mitchell, J. F.
969 B., Nakicenovic, N., Riahi, K., Smith, S. J., Stouffer, R. J., Thomson, A. M.,
970 Weyant, J. P., and Wilbanks, T. J.: The next generation of scenarios for climate
971 change research and assessment, *Nature*, 463, 747-756, doi:10.1038/nature08823,

972 2010.

973 Nakajima, T., Tsukamoto, M., Tsushima, Y., Numaguti, A., and Kimura, T.: Modeling
974 of the radiative process in an atmospheric general circulation model, *Appl. Optics*,
975 39, 4869–4878, doi:10.1364/AO.39.004869, 2000.

976 Nakanishi, M. and Niino, H.: An improved Mellor–Yamada level 3 model with
977 condensation physics: Its design and verification, *Bound.-Lay. Meteorol.*, 112, 1-31,
978 doi:10.1023/B:BOUN.0000020164.04146.98, 2004.

979 Nakanishi, M. and Niino, H.: Development of an improved turbulence closure model
980 for the atmospheric boundary layer, *J. Meteorol. Soc. Japan*, 87, 895-912,
981 doi:10.2151/jmsj.87.895, 2009.

982 Nasuno, T.: Forecast skill of Madden-Julian Oscillation events in a global
983 nonhydrostatic model during the CINDY2011/DYNAMO observation period,
984 *SOLA*, 9, 69-73, doi:10.2151/sola.2013-016, 2013.

985 Niwa, Y., Tomita, H., Satoh, M., and Imasu, R.: A three-dimensional icosahedral grid
986 advection scheme preserving monotonicity and consistency with continuity for
987 atmospheric tracer transport, *J. Meteorol. Soc. Jpn.*, 89, 255-268,
988 doi:10.2151/jmsj.2011-306, 2011.

989 Noda, A. T., Oouchi, K., Satoh, M., Tomita, H., Iga, S., and Tsushima, Y.: Importance
990 of the subgrid-scale turbulent moist process of the turbulent transport: On cloud
991 distribution in global cloud-resolving simulations, *Atmos. Res.*, 96, 208-217,
992 doi:10.1016/j.atmosres.2009.05.007, 2009.

993 Ohara, T., Akimoto, H., Kurokawa, J., Horii, N., Yamaji, K., Yan, X., and Hayasaka,

994 T.: An Asian emission inventory of anthropogenic emission sources for the period
995 1980-2020, *Atmos. Chem. Phys.*, 7, 4419-4444, 2007.

996 Okamoto, K., Iguchi, T., Takahashi, N., Iwanami, K., and Ushio, T.: The global satellite
997 mapping of precipitation (GSMaP) project, 25th IGARSS Proceedings, 3414-3416,
998 2005.

999 Pope III, C. A., Ezzati, M., and Dockery, D. W.: Fine-particulate air pollution and life
1000 expectancy in the United States, *N. Engl. J. Med.*, 360, 376-386,
1001 doi:10.1056/NEJMsa0805646, 2009.

1002 Ramanathan, V., Akimoto, H., Bonasoni, P., Brauer, M., Carmichael, G., Chung, C. E.,
1003 Feng, Y., Fuzzi, S., Hasnain, S. I., Iyengararasan, M., Jayaraman, A., Lawrence, M.
1004 G., Nakajima, T., Panwar, T. S., Ramana, M. V., Rupakheti, M., Weidemann, S.,
1005 and Yoon, S.-C.: Atmosphere brown clouds and regional climate change, part I of
1006 atmosphere brown clouds: Regional assessment report with focus on Asia, Project
1007 Atmosphere Brown Cloud, United National Environment Programme, Nairobi,
1008 Kenya, 2008.

1009 Randall, D. A., Heikes, R., and Ringler, T.: Global atmospheric modeling using a
1010 geodesic grid with an isentropic vertical coordinate, in: *General Circulation Model
1011 Development*, Academic Press, San Diego, CA, 509-538, 2000.

1012 Saito, K., Fujita, T., Yamada, Y., Ishida, J., Kumagai, Y., Aranami, K., Ohmori, S.,
1013 Nagasawa, R., Kumagai, S., Muroi, C., Kato, T., Eito, H., and Yamazaki, Y.: The
1014 Operational JMA Nonhydrostatic Mesoscale Model, *Mon. Wea. Rev.*, 134,
1015 1266-1298, doi: [hyyp://dx.doi.org/10.1175/MWR3120.1](https://doi.org/10.1175/MWR3120.1), 2006.

1016 Sato, T., Miura, H., Satoh, M., Takayabu, Y. N., and Wang, Y.: Diurnal cycle of
1017 precipitation in the tropics simulated in a global cloud-resolving model, *J. Climate*,
1018 22, 4809-4826; doi:10.1175/2009JCLI2890.1, 2009.

1019 Satoh, M., Matsuno, T., Tomita, H., Miura, H., Nasuno, T., and Iga, S.: Nonhydrostatic
1020 Icosahedral Atmospheric Model (NICAM) for global cloud resolving simulations, *J.*
1021 *Comput. Phys.*, 227, 3486-3514, doi:10.1016/j.jcp.2007.02.006, 2008.

1022 Satoh, M., Inoue, T., and Miura, H.: Evaluations of cloud properties of global and local
1023 cloud system resolving models using CALIPSO and CloudSat simulators, *J.*
1024 *Geophys. Res.*, 115, D00H14, doi:10.1029/2009JD012247, 2010.

1025 Satoh, M., Tomita, H., Yashiro, H., Miura, H., Kodama, C., Seiki, T., Noda, A.,
1026 Yamada, T., Goto, D., Sawada, M., Miyoshi, T., Niwa, Y., Hara, M., Ohno, T., Iga,
1027 S., Arakawa, T., Inoue, T., and Kubokawa, H.: The Non-hydrostatic icosahedral
1028 atmospheric model: description and development, *Progress in Earth and Planetary*
1029 *Science*, 1, 18-49, doi:10.1186/s40645-014-0018-1, 2014.

1030 Schutgens, N., Nakata, M., and Nakajima, T.: Estimating aerosol emissions by
1031 assimilating remote sensing observations into a global transport model, *Remote*
1032 *Sens.*, 4, 3528-3542, doi:10.3390/rs4113528, 2012.

1033 Seiki, T. and Nakajima, T.: Aerosol effects of the condensation process on a convective
1034 cloud simulation, *J. Atmos. Sci.*, 71, 833-853, doi:10.1175/JAS-D-12-0195.1,
1035 2014.

1036 Sekiguchi, M. and Nakajima, T.: A *k*-distribution-based radiation code and its
1037 computational optimization for an atmospheric general circulation model, *J. Quant.*

1038 Spectrosc. RA, 109, 2779-2793, doi:10.1016/j.jqsrt.2008.07.013, 2008.

1039 Shimadera, H., Hayami, H., Morino, Y., Ohara, T., Chatani, S., Hasegawa, S., and
1040 Kaneyasu, N.: Analysis of summertime atmospheric transport of fine particulate
1041 matter in northeast Asia, *Asia-Pac. J. Atmos. Sci.*, 49, 347-360,
1042 doi:10.1007/s13143-013-0033-y, 2013.

1043 Shimizu, A., Sugimoto, N., Matsui, I., Arao, K., Uno, I., Murayama, T., Kagawa, N.,
1044 Aoki, K., Uchiyama, A., and Yamazaki, A.: Continuous observations of Asian dust
1045 and other aerosols by polarization lidars in China and Japan during ACE-Asia, *J.*
1046 *Geophys. Res.*, 109, D19S17, doi: 10.1029/2002JD003253, 2004.

1047 Stuhne, G. R. and Peltier, W. R.: Vortex erosion and amalgamation in a new model of
1048 large scale flow on the sphere, *J. Comput. Phys.* 128, 58-81,
1049 doi:10.1006/jcph.1996.0196, 1996.

1050 Sudo, K., Takahashi, M., Kurokawa, J., and Akimoto, H.: CHASER: A global chemical
1051 model of the troposphere: 1. Model description, *J. Geophys. Res.*, 107, 4339,
1052 doi:10.1029/2001JD001113, 2002.

1053 Sugimoto, N., Uno, I., Nishikawa, M., Shimizu, A., Matsui, I., Dong, X., Chen, Y.,
1054 Quan, H.: Record Heavy Asian Dust in Beijing in 2002: Observations and Model
1055 Analysis of Recent Events, *Geophys. Res. Lett.* 30(12), 1640,
1056 doi:10.1029/2002GL016349, 2003.

1057 Suzuki, K., Nakajima, T., Satoh, M., Tomita, H., Takemura, T., Nakajima, T. Y., and
1058 Stephens, G. L.: Global cloud-system-resolving simulation of aerosol effect on
1059 warm clouds, *Geophys. Res. Lett.*, 35, L19817, doi:10.1029/2008GL035449, 2008.

1060 Takemura, T.: Distributions and climate effects of atmospheric aerosols from the
1061 preindustrial era to 2100 along Representative Concentration Pathway (RCPs)
1062 simulated using the global aerosol model SPRINTARS, *Atmos. Chem. Phys.*, 12,
1063 11555-11572, doi:10.5194/acp-12-11555-2012, 2012.

1064 Takemura, T., Okamoto, H., Maruyama, Y., Numaguti, A., Higurashi, A., and Nakajima,
1065 T.: Global three-dimensional simulation of aerosol optical thickness distribution of
1066 various origins, *J. Geophys. Res.*, 105, 17853-17873, doi:10.1029/2000JD900265,
1067 2000.

1068 Takemura, T., Nakajima, T., Dubovik, O., Holben, B. N., and Kinne, S.: Single
1069 scattering albedo and radiative forcing of various aerosol species with a global
1070 three-dimensional model, *J. Climate*, 15, 333-352,
1071 doi:10.1175/1520-0442(2002)015<0333:SSAARF>2.0.CO;2, 2002.

1072 Takemura, T., Nozawa, T., Emori, S., Nakajima, T. Y., and Nakajima, T.: Simulation of
1073 climate response to aerosol direct and indirect effects with aerosol
1074 transport-radiation model, *J. Geophys. Res.*, 110, D02202,
1075 doi:10.1029/2004JD005029, 2005.

1076 Taylor, M., Tribbia, J., and Iskandarani, M.: The spectral element method for the
1077 shallow water equations on the sphere, *J. Comput. Phys.* 130, 92-108,
1078 doi:10.1006/jcph.1996.5554,1997.

1079 Textor, C. Schulz, M., Guibert, S., Kinne, S., Balkanski, Y., Bauer, S., Berntsen, T.,
1080 Berglen, T., Boucher, O., Chin, M., Dentener, F., Diehl, T., Easter, R., Feichter, J.,
1081 Fillmore, D., Ghan, S., Ginoux, P., Gong, S., Grini, A., Hendricks, J., Horowitz, L.,

1082 Huang, P., Isaksen, I., Iversen, T., Kloster, S., Koch, D., Kirkevåg, A., Kristjansson,
1083 J. E., Krol, M., Lauer, A., Lamarque, J. F., Liu, X., Montanaro, V., Myhre, G.,
1084 Penner, J. E., Pitari, G., Reddy, S., Seland, Ø., Stier, P., Takemura, T., and Tie, X.:
1085 Analysis and quantification of the diversities of aerosol life cycles within AeroCom,
1086 *Atmos. Chem. Phys.*, 6, 1777-1813, doi:10.5194/acp-6-1777-2006, 2006.

1087 Turpin, B. J., and Lim, H.-J.: Species contributions to PM_{2.5} mass concentrations:
1088 revisiting common assumptions for estimating organic mass, *Aerosol Sci. Tech.*, 35,
1089 602-610, doi: 10.1080/02786820119445, 2001.

1090 Tomita, H.: A stretched grid on a sphere by new grid transformation, *J. Meteorol. Soc.*
1091 *Jpn.*, 86A, 107-119, 2008a.

1092 Tomita, H.: New microphysics with five and six categories with diagnostic generation
1093 of cloud ice, *J. Meteorol. Soc. Jpn.*, 86A, 121-142, 2008b.

1094 Tomita, H. and Satoh, M.: A new dynamical framework of nonhydrostatic global
1095 model using the icosahedral grid, *Fluid Dyn. Res.*, 34, 357-400, 2004.

1096 Tomita, H., Miura, H., Iga, S., Nasuno, T., and Satoh, M.: A global cloud-resolving
1097 simulation: Preliminary results from an aqua planet experiment, *Geophys. Res.*
1098 *Lett.*, 32, L08805, doi:10.1029/2005GL022459, 2005.

1099 Tomita, H., K. Goto, and Satoh, M.: A new approach of atmospheric general circulation
1100 model: Global cloud resolving model NICAM and its computational performance,
1101 *SIAM J. Sci. Stat. Comp.*, 30, 2755-2776, doi:10.1137/070692273, 2008.

1102 Ueda, K., Nitta, H., Ono, M., and Takeuchi, A.: Estimating mortality effects of fine
1103 particulate matter in Japan: A comparison of time-series and case-crossover

1104 analysis, *J. Air and Water Manage. Assoc.*, 59, 1212-1218,
1105 doi:10.3155/1047-3289.59.10.1212, 2009.

1106 UNEP and WMO: Integrated assessment of black carbon and tropospheric ozone,
1107 United Nations Environment Programme (UNEP) and World Meteorological
1108 Organization (WMO), Nairobi, Kenya, 2011.

1109 Ushio, T., Kubota, T., Shige, S., Okamoto, K., Aonashi, K., Inoue, T., Takahashi, N.,
1110 Iguchi, T., Kachi, M., Oki, R., Morimoto, T., and Kawasaki, Z.: A Kalman filter
1111 approach to the Global Satellite Mapping of Precipitation (GSMaP) from combined
1112 passive microwave and infrared radiometric data. *J. Meteor. Soc. Japan*, 87A,
1113 137-151, 2009.

1114 Wang, J., Xun X. Q., Henze, D. K., Zeng, J., Ji, Q., Tsay, S.-C., and Huang, J. P.:
1115 Top-down estimate of dust emissions through integration of MODIS and MISR
1116 aerosol retrievals with the GEOS-Chem adjoint model, *Geophys. Res. Lett.*, 39(8),
1117 DOI: 10.1029/2012GL051136, 2012.

1118 Watanabe, M., Suzuki, T., O'ishi, R., Komuro, Y., Watanabe, S., Emori, S., Takemura,
1119 T., Chikira, M., Ogura, T., Sekiguchi, M., Takata, K., Yamazaki, D., Yokohata, T.,
1120 Nozawa, T., Hasumi, H., Tatebe, H., and Kimoto, M.: Improved climate simulation
1121 by MIROC 5: Mean states, variability, and climate sensitivity, *J. Climate*, 23,
1122 6312-6335, 2010.

1123 Xu, X. Q., Wang, J., Henze, D. K., Qu, W. J., and Kopacz, M.: Constraints on aerosol
1124 source using GEOS-Chem adjoint and MODIS radiances, and evaluation with
1125 multisensor (OMI, MISR) data *J. Geophys. Res. Atmos.*, 118 (12), 6396-6413,

1126 DOI: 10.1002/jgrd.50515, 2013.

1127 Yu, H., Remer, L. A., Chin, M., Bian, H., Tan, Q., Yuan, T., and Zhang, Y.: Aerosols
1128 from overseas rival domestic emissions over North America, *Science*, 337, 566-569,
1129 doi:10.1126/science.1217576, 2012.

1130 Yumimoto, K. and Takemura T.: The SPRINTARS/4D-Var Data Assimilation System:
1131 Development and Inversion Experiments Based on the Observing System
1132 Simulation Experiment Framework, *Geosci. Model Dev.*, 6, 2005-2022,
1133 doi:10.5194/gmd-6-2005-2013, 2013.

1134 Zhang, Q., Jimenez, J. L., Canagaratna, M. R., Allan, J. D., Coe, H., Ulbrich, I., Alfarra,
1135 M. R., Takami, A., Middlebrook, A. M., Sun, Y. L., Dzepina, K., Dunlea, E.,
1136 Docherty, K., DeCarlo, P. F., Salcedo, D., Onasch, T., Jayne, J. T., Miyoshi, T.,
1137 Shimono, A., Hatakeyama, S., Takegawa N., Kondo, Y., Schneider, J., Drewnick,
1138 F., Borrmann, S., Weimer, S., Demerjian, K., Williams, P., Bower, K., Bahreini, R.,
1139 Cottrell, L., Griffin, R. J., Rautiainen, J., Sun, J. Y., Zhang, Y. M., and Worsnop, D.
1140 R.: Ubiquity and dominance of oxygenated species in organic aerosols in
1141 anthropogenically-influenced Northern Hemisphere midlatitudes, *Geophys. Res.
1142 Lett.*, 34, L13801, doi:10.1029/2007GL029979, 2007.

1143 Zhang, X. Y., Wang, Y. Q., Niu, T., Zhang, X. C., Gong, S. L., Zhang, Y. M., and Sun,
1144 J. Y.: Atmospheric aerosol compositions in China: spatial/temporal variability,
1145 chemical signature, regional haze distribution and comparisons with global aerosols,
1146 *Atmos. Chem. Phys.*, 12, 779-799, doi: 10.5194/acp-12-779-2012, 2012.

1147 Table 1. Statistical values (averages of the observation and simulations, correlation
 1148 coefficient R and root-mean-square-error $RMSE$) for meteorological fields using the
 1149 simulations (NICAM-g6str and NICAM-g6) and observations at seven sites during the
 1150 same period, as shown in Figures 4 to 7.

		Yokohama	Chiba	Tsuchiura	Adachi	Maebashi	Machida	Kisai
		Temperature						
Average [°C] and difference [°C] (vs. observati on) in bracket	Observation	27.9	30.1	28.1	29.7	29.1	29.1	27.9
	NICAM-g6str	26.9 (-1.1)	28.3 (-1.8)	28.3 (0.2)	27.3 (-2.3)	25.5 (-3.6)	25.9 (-3.2)	25.8 (-2.2)
	NICAM-g6	25.5 (-2.4)	26.2 (-3.9)	25.7 (-2.4)	25.5 (-4.1)	23.9 (-5.2)	25.5 (-3.6)	23.9 (-4.0)
R	NICAM-g6str	0.74	0.85	0.84	0.81	0.79	0.74	0.80
	NICAM-g6	0.76	0.67	0.79	0.78	0.71	0.77	0.75
RMSE [°C]	NICAM-g6str	1.9	2.3	1.9	3.0	4.3	3.9	3.0
	NICAM-g6	2.8	4.4	3.1	4.6	5.8	4.0	4.6
		RH						
Average [%] and difference [%] (vs. observati on) in bracket	Observation	73.5	79.0	73.3	75.4	73.7	75.9	71.4
	NICAM-g6str	83.6 (10.0)	77.5 (-1.5)	76.4 (3.0)	77.9 (2.5)	82.7 (9.0)	82.5 (6.6)	81.6 (10.1)
	NICAM-g6	92.2 (18.6)	92.4 (13.4)	93.4 (20.0)	92.2 (16.8)	95.5 (21.9)	92.2 (16.3)	95.5 (24.1)
R	NICAM-g6str	0.64	0.68	0.69	0.72	0.72	0.72	0.81
	NICAM-g6	0.73	0.59	0.79	0.82	0.71	0.74	0.76
RMSE [%]	NICAM-g6str	12.7	8.9	11.0	10.1	14.6	12.9	13.3
	NICAM-g6	19.5	16.2	22.4	19.8	25.5	20.1	26.3
		Wind speed						
Average [m/s] and	Observation	2.9	2.6	1.6	2.6	1.2	2.7	1.9
	NICAM-g6str	4.2	3.8	3.1	3.4	3.1	3.0	2.7

difference [m/s] (vs. observati on) in bracket		(1.3)	(1.1)	(1.4)	(0.9)	(1.9)	(0.3)	(0.8)
	NICAM-g6	3.7 (0.7)	5.0 (2.4)	1.0 (-0.7)	3.7 (1.1)	0.9 (-0.4)	3.7 (1.0)	0.9 (-1.0)
R	NICAM-g6str	0.72	0.41	0.65	0.51	0.19	0.59	0.16
	NICAM-g6	0.64	0.43	0.38	0.47	0.12	0.53	0.04
RMSE [m/s]	NICAM-g6str	1.9	2.0	1.8	1.7	2.3	1.3	1.7
	NICAM-g6	1.4	3.0	1.2	1.7	0.7	1.7	1.4

1151

1152 Table 2. Statistical values (averages of the observation and simulations, correlation
1153 coefficient R and root-mean-square-error $RMSE$) for EC, sulfate, and SO_2
1154 concentrations by the simulations (NICAM-g6str, NICAM-g6, and WRF-CMAQ) and
1155 the observations at four FAMIKA sites during the period from August 6 to 11. The
1156 WRF-CMAQ results are given by Shimadera et al. (2013).

		Maebashi	Kisai	Komae	Tsukuba
		EC			
Average [$\mu\text{g}/\text{m}^3$] and difference [%] (vs. observation) in bracket	Observation	2.85	2.75	1.23	2.20
	NICAM-g6str	0.39 (-86)	0.60 (-78)	1.10 (-10)	0.73 (-67)
	NICAM-g6	0.52 (-82)	0.52 (-81)	0.49 (-60)	0.58 (-74)
	WRF-CMAQ	0.87 (-69)	1.17 (-58)	0.92 (-25)	0.77 (-65)
R	NICAM-g6str	-0.02	0.41	0.55	0.59
	NICAM-g6	-0.49	-0.28	-0.05	0.16
	WRF-CMAQ	0.08	0.33	0.37	-0.23
RMSE [$\mu\text{g}/\text{m}^3$]	NICAM-g6str	2.62	2.33	0.72	1.85
	NICAM-g6	2.52	2.45	1.10	2.06
	WRF-CMAQ	2.18	1.83	0.88	1.98
		Sulfate			
Average [$\mu\text{g}/\text{m}^3$] and difference [%] (vs. observation) in bracket	Observation	4.79 (-6)	2.86 (44)	4.18 (-32)	4.85 (-12)
	NICAM-g6str	4.51 (-34)	4.14 (11)	2.84 (-46)	4.25 (-26)
	NICAM-g6	3.17 (-21%)	3.17 (42%)	2.25 (-21%)	3.58 (-22%)
	WRF-CMAQ	3.77	4.08	3.30	3.80

R	NICAM-g6str	0.01	0.50	0.51	0.73
	NICAM-g6	0.05	0.56	0.86	0.75
	WRF-CMAQ	0.41	0.02	0.87	0.78
RMSE [$\mu\text{g}/\text{m}^3$]	NICAM-g6str	3.61	2.81	2.71	2.49
	NICAM-g6	3.01	2.30	2.49	2.77
	WRF-CMAQ	2.30	3.37	1.62	2.56
		SO_2			
Average [ppbv]	Observation	2.74	2.28	2.35	3.79
and difference [%] (vs. observation) in bracket	NICAM-g6str	1.25 (-54)	1.90 (-17)	2.34 (-1)	2.34 (-38)
	NICAM-g6	2.42 (-12)	2.45 (7)	2.52 (7)	3.21 (-15)
R	NICAM-g6str	0.02	-0.04	0.62	0.21
	NICAM-g6	-0.64	-0.52	0.22	-0.04
RMSE [ppbv]	NICAM-g6str	1.82	0.93	0.97	2.08
	NICAM-g6	1.29	0.94	0.85	1.29

1157

1158 Table 3. PM_{2.5} concentrations in daily, daytime (from 9 am to 4 pm), and nighttime
1159 (from 9 pm to 4 am) averages and mean ratios of daytime to nighttime using the
1160 simulations (NICAM-g6str and NICAM-g6) and the observation at selected seven sites
1161 in August.

	Maebashi	Kawasaki	Toride	Hasuda	Sapporo	Nagoya	Fukuoka
	Daily mean PM _{2.5} [$\mu\text{g}/\text{m}^3$] and standard deviation [$\mu\text{g}/\text{m}^3$]						
Observation	24.9±12.8	23.2±12.9	17.6±9.7	20.6±11.5	12.7±6.3	17.3±10.1	14.3±7.5
NICAM-g6str	6.4±3.9	10.0±7.3	9.0±6.3	8.4±5.0	4.9±3.5	7.5±5.7	3.4±2.6
NICAM-g6	6.7±3.0	6.7±3.3	6.7±3.4	6.7±3.0	4.7±4.1	5.4±3.0	3.5±2.3
	Daytime (9am-4pm) mean PM _{2.5} [$\mu\text{g}/\text{m}^3$] and standard deviation [$\mu\text{g}/\text{m}^3$]						
Observation	28.6±14.1	19.4±12.1	15.8±9.0	21.0±10.0	15.0±5.2	11.3±5.4	9.7±5.7
NICAM-g6str	5.9±3.8	7.1±4.3	6.8±4.4	7.2±4.5	5.3±2.8	3.5±2.3	1.6±0.8
NICAM-g6	5.0±1.7	4.0±2.1	4.0±2.4	4.4±1.9	7.4±4.5	2.4±0.9	1.4±0.5
	Nighttime (9pm-4am) mean PM _{2.5} [$\mu\text{g}/\text{m}^3$] and standard deviation [$\mu\text{g}/\text{m}^3$]						
Observation	24.4±11.9	24.5±11.8	16.9±9.6	18.5±10.3	10.7±6.6	19.1±8.2	15.4±6.7
NICAM-g6str	7.5±3.6	14.2±9.2	12.1±7.6	10.8±5.5	4.1±3.9	12.0±4.6	5.1±3.1

NICAM-g6	7.5±2.3	9.1±1.5	8.8±2.1	8.4±3.0	2.6±3.1	7.8±1.3	4.4±2.2
	Ratio of daytime-mean PM2.5 to nighttime-mean PM2.5						
Observation	1.8±0.8	1.7±0.5	1.3±0.4	1.2±0.4	1.0±0.4	1.3±0.4	1.1±0.3
NICAM-g6str	1.1±0.6	1.3±0.7	1.1±0.6	1.1±0.5	0.9±0.3	1.2±0.9	1.0±0.6
NICAM-g6	0.9±0.2	0.8±0.1	0.8±0.1	0.8±0.1	0.8±0.2	0.9±0.2	0.8±0.2

1162

1163 **Figure captions**

1164 Figure 1 Topographical maps of (a) East Asia and (b) Eastern Japan, including the
1165 observation sites for the model validation. The topography is based on GTOPO30 (the
1166 horizontal resolution is 30 arc seconds, that is approximately 1 km) courtesy of the U.S.
1167 Geological Survey.

1168

1169 Figure 2 (a) EC and (b) SO₂ emission inventories in 2007.

1170

1171 Figure 3 Horizontal distributions of temperature and winds in August averages at the
1172 surface and the model height of approximately 5 km for the model bottom of MSL over
1173 Asia region using reanalysis data from NCEP-FNL, simulation by NICAM-g6str, and
1174 simulation by NICAM-g6.

1175

1176 Figure 4 Temporal variations in the NICAM-g6str and NICAM-g6 simulated and
1177 observed air temperature for a height of 2 m at (a) Yokohama, (b) Chiba, (c) Tsuchiura,
1178 (d) Adachi, (e) Maebashi, (f) Machida and (g) Kisai in August 2007.

1179

1180 Figure 5 Same as Figure 4 but for relative humidity (RH).

1181

1182 Figure 6 Same as Figure 4 but for wind direction.

1183

1184 Figure 7 Same as Figure 4 but for wind speed.

1185

1186 Figure 8 Horizontal distributions of precipitation in August averages derived from (a)
1187 simulation by NICAM-g6str, (b) simulation by NICAM-g6, (c) reanalysis data from
1188 MSM by JMA and (d) reanalysis data from GSMaP.

1189

1190 Figure 9 Temporal variations in the NICAM-g6str and NICAM-g6 simulated and
1191 observed precipitation amounts at 21 Japanese sites in August 2007. The comparison
1192 includes 10 sites in the Kanto area; (a) Maebashi, (b) Konosu, (c) Huchu, (d) Tsukuba,
1193 (e) Tokyo, (f) Yokohama, (g) Abiko, (h) Saitama, (i) Chiba, and (j) Nerima, 3 sites in
1194 the northern Japan; (k) Niigata, (l) Sendai, and (m) Sapporo, 5 sites in the western
1195 Japan; (n) Nagoya, (o) Osaka, (p) Himeji, (q) Fukuoka, and (r) Hyuga, and 3 remote
1196 islands (s) Hachijo-jima, (t) Oshima, and (u) Naha.

1197

1198 Figure 10 Predictive values of daily precipitation using the NICAM-g6str and
1199 NICAM-g6 simulations and the AMeDAS measurements during August 2007 at the
1200 sites defined at Figure 9, in units of percentage.

1201

1202 Figure 11 Temporal variations in the simulated (NICAM-g6str, NICAM-g6, and
1203 WRF-CMAQ) and observed EC mass concentrations near the surface at (a) Maebashi,
1204 (b) Kisai, (c) Komae and (d) Tsukuba in August 2007. The WRF-CMAQ results are
1205 given by Shimadera et al. (2013). The left axis in red represents the simulated values,
1206 and the right axis in black represents the observed values, in units of $\mu\text{g}/\text{m}^3$.

1207

1208 Figure 12 Same as Figure 11 but for sulfate.

1209

1210 Figure 13 Same as Figure 12 but for SO₂ without the WRF-CMAQ results, in units of
1211 ppbv.

1212

1213 Figure 14 Scatterplot of August mean concentrations for EC, sulfate and SO₂ between
1214 the simulations by NICAM-g6str and NICAM-g6 and the observations at the sites
1215 shown in the left panels.

1216

1217 Figure 15 Horizontal distributions of concentrations for EC, sulfate and SO₂ near the
1218 surface using NICAM-g6str and NICAM-g6 in August averages. The circles in color
1219 shows the observation results at the sites.

1220

1221 Figure 16 (a) EC and (b) sulfate mass concentrations at the FAMIKA four sites using
1222 NICAM-g6str under the sensitivity experiments, WRF-CMAQ results shown by
1223 Shimadera et al. (2013) and the FAMIKA observations in averages of August 6-11. The
1224 bar represents the range of the sensitivity.

1225

1226 Figure 17 Temporal variations in the NICAM-g6str and NICAM-g6 simulated and
1227 observed PM_{2.5} near the surface at 18 Japanese sites in August 2007. The left axis in
1228 red represents the simulated values, and the right axis in black represents the observed

1229 values, in unit of μgm^{-3} .

1230

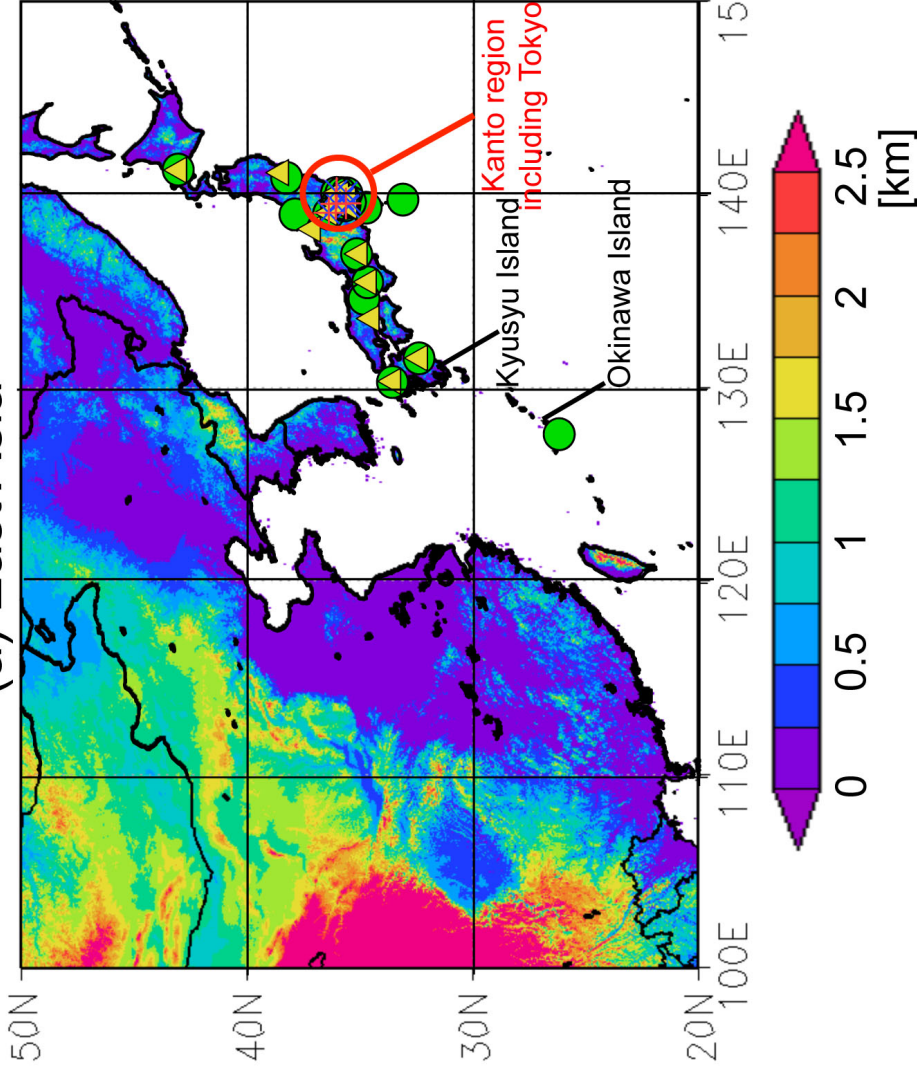
1231 Figure 18 Extinction coefficients in August averages for the spherical particles

1232 simulated by NICAM-g6str and NICAM-g6 and the spherical particles observed by the

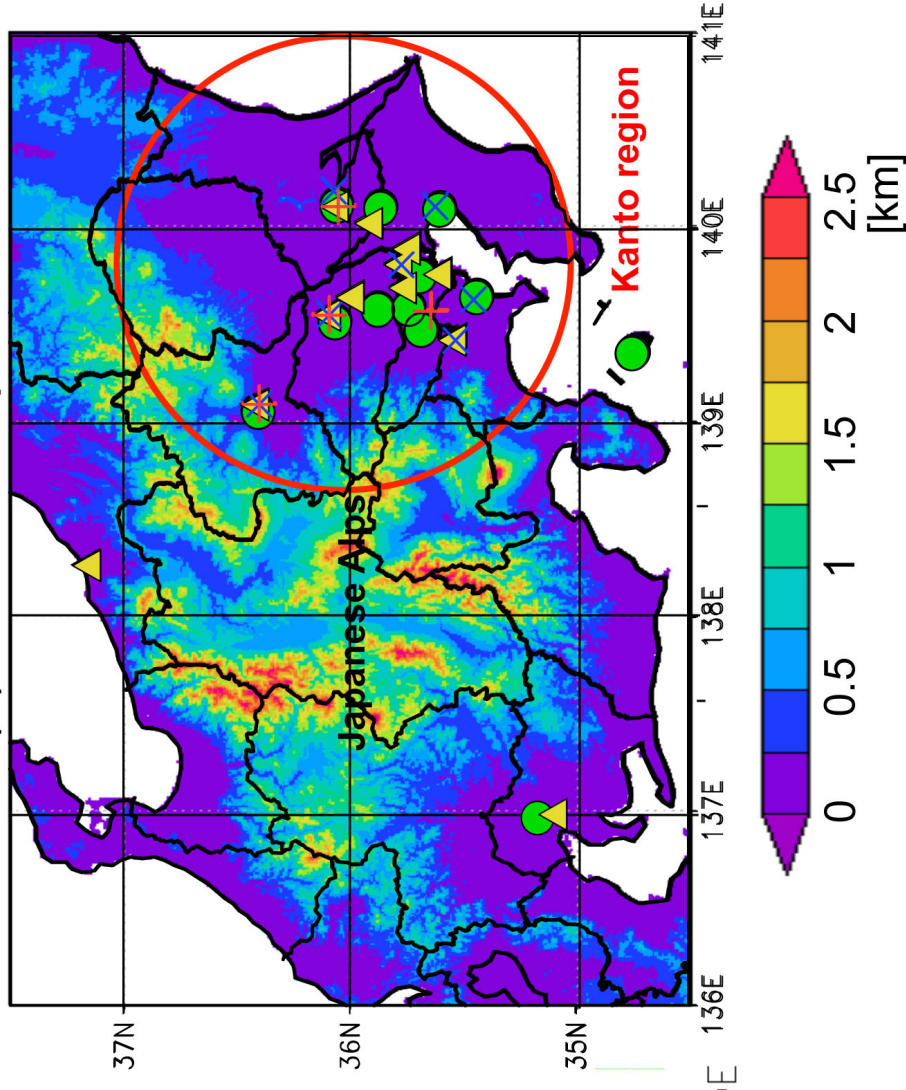
1233 NIES-LIDAR network at (a) Tsukuba and (b) Chiba, in units of $1/(\text{Mm})$. The bars

1234 represent the 25th and 75th percentiles of the LIDAR observations.

(a) East Asia



(b) Eastern Japan



+ : FAMIKA sites (Aerosol chemical species) including 4 sites; Maebashi (139.10°E, 36.40°N),
Kisai (139.56°E, 36.09°N), Komae (139.58°E, 35.64°N), Tsukuba (140.12°E, 36.05°N)

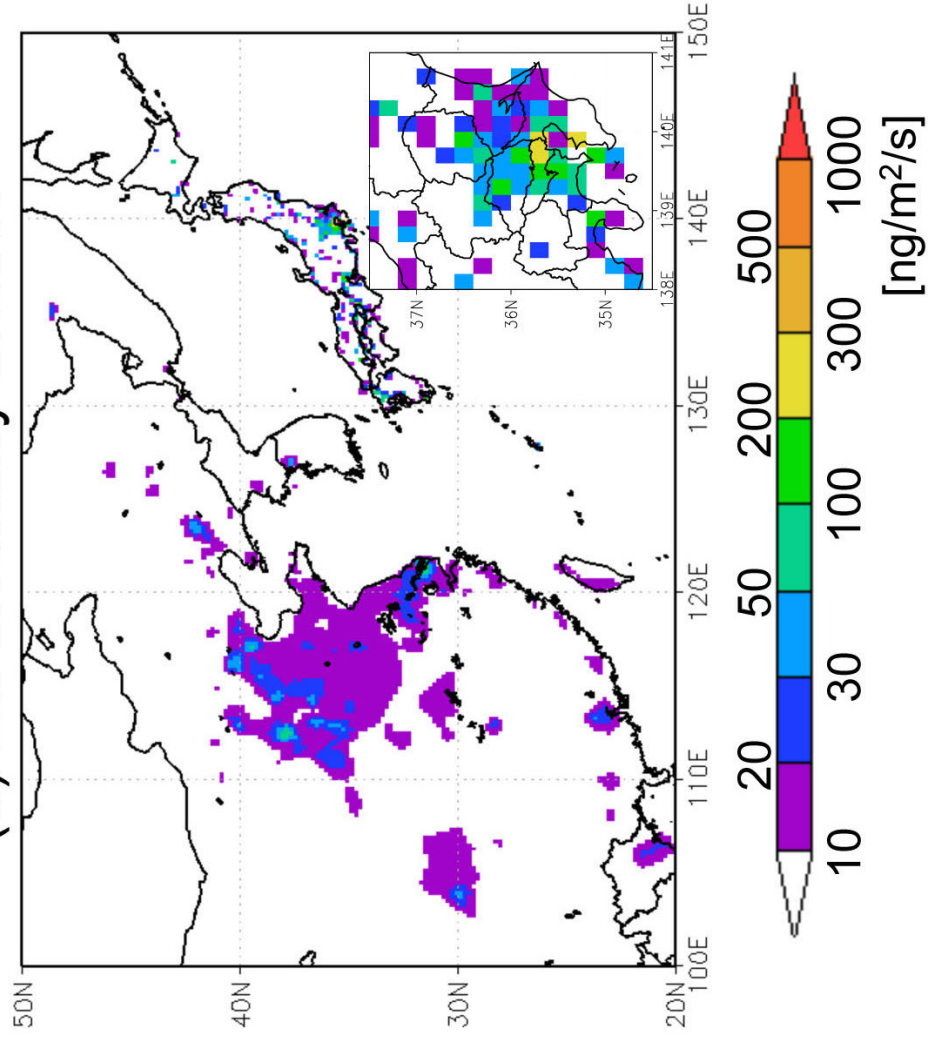
X : 7 Sites (Meteorology measurements)

● : 21 Sites (Precipitation measurements by AMeDAS)

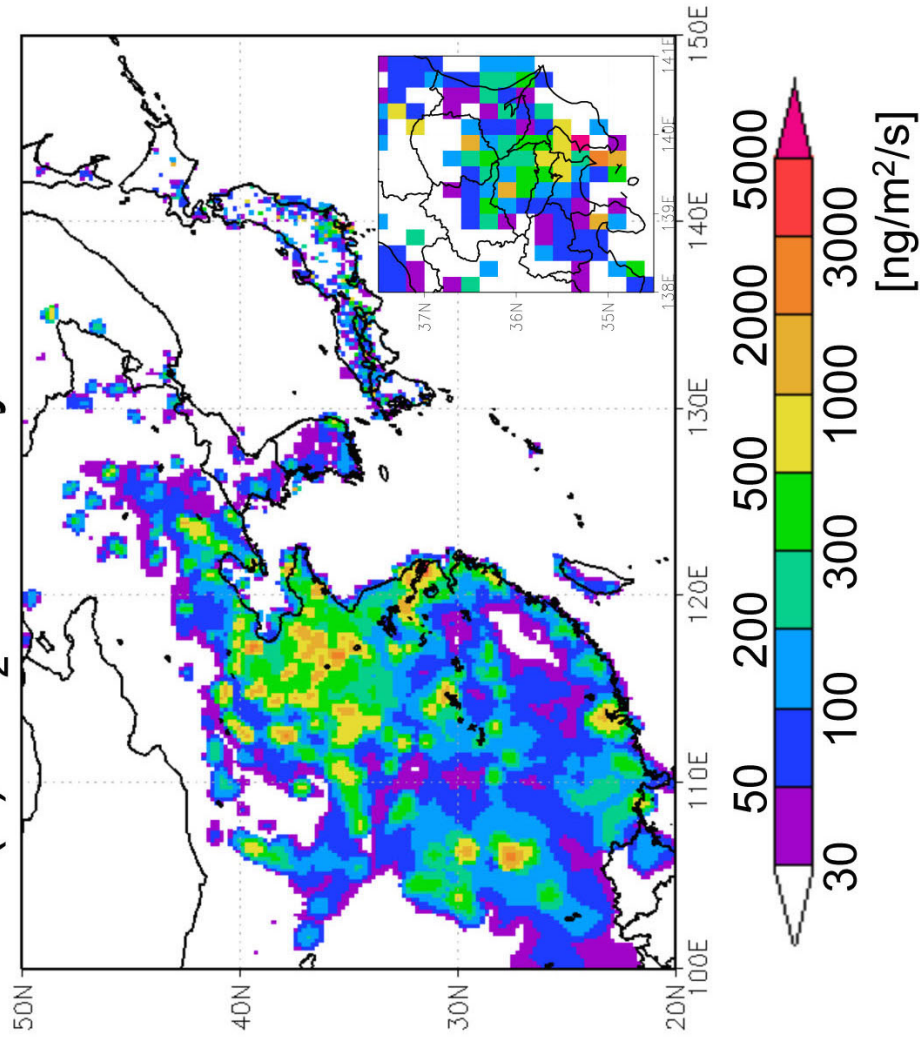
▲ : 18 Sites (PM_{2.5} measurements)

□ : 2 Sites (LIDAR measurements)

(a) EC inventory in 2007

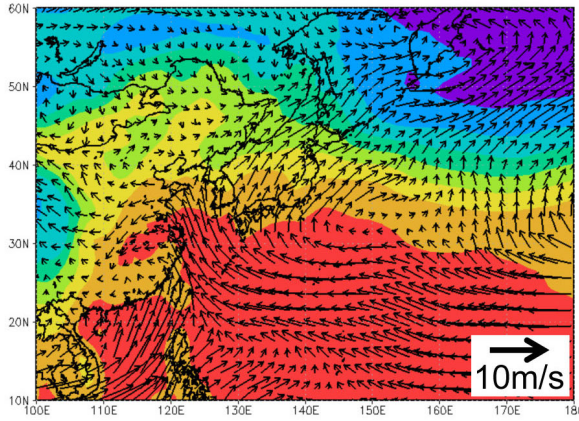


(b) SO₂ inventory in 2007

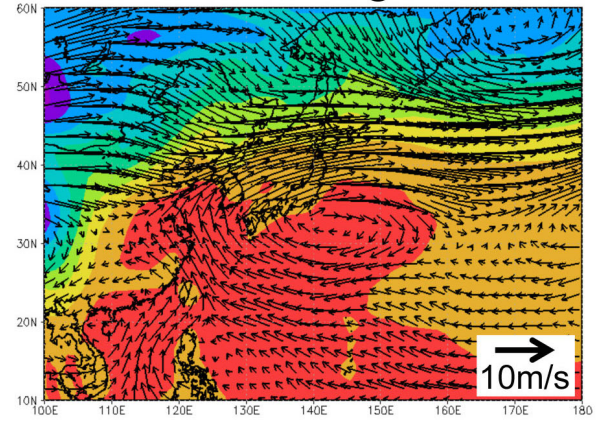


NCEP-FNL

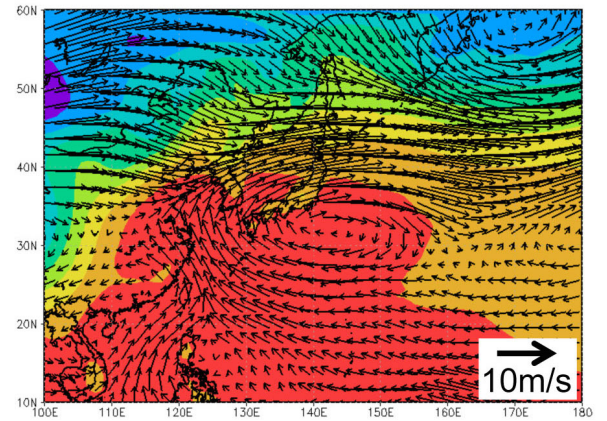
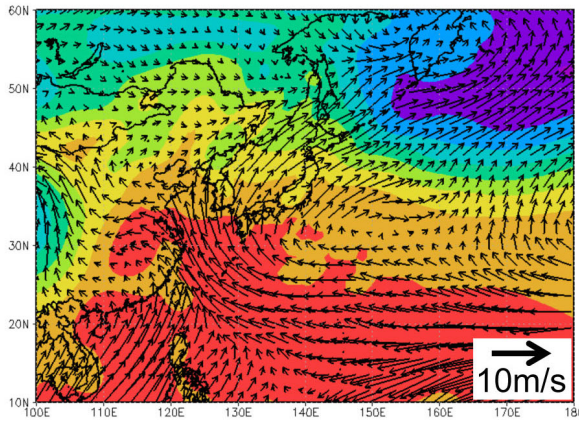
Surface



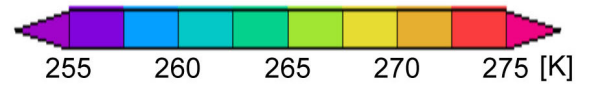
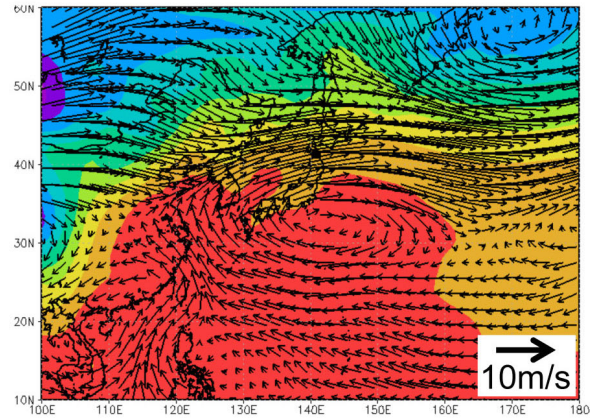
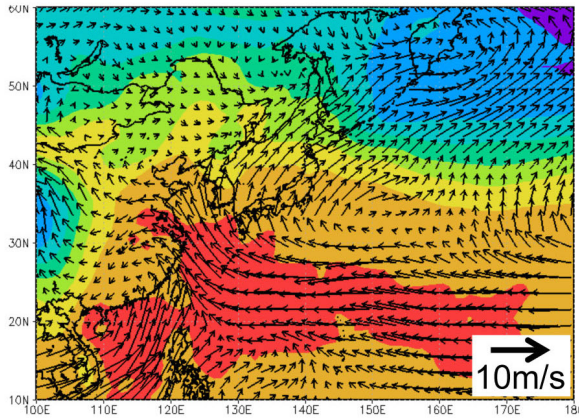
5km height

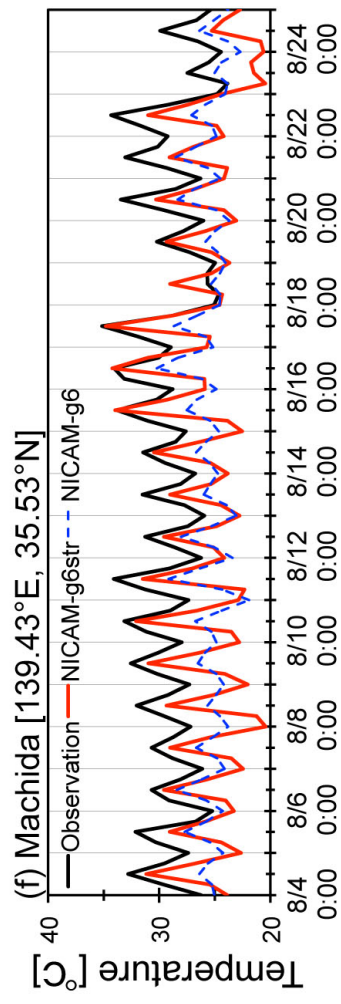
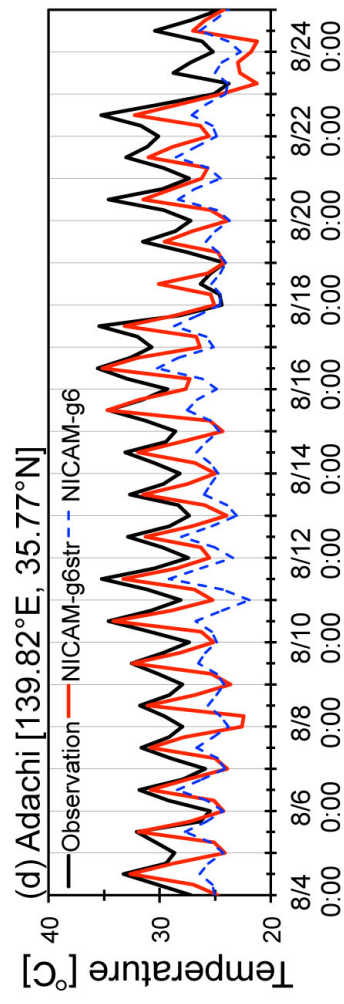
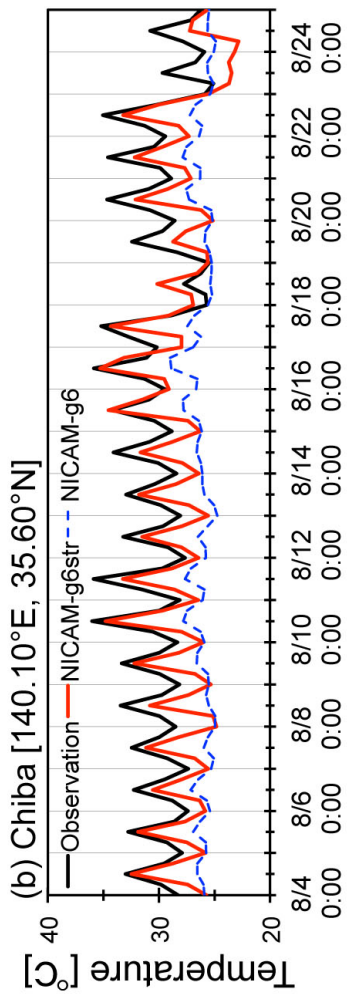
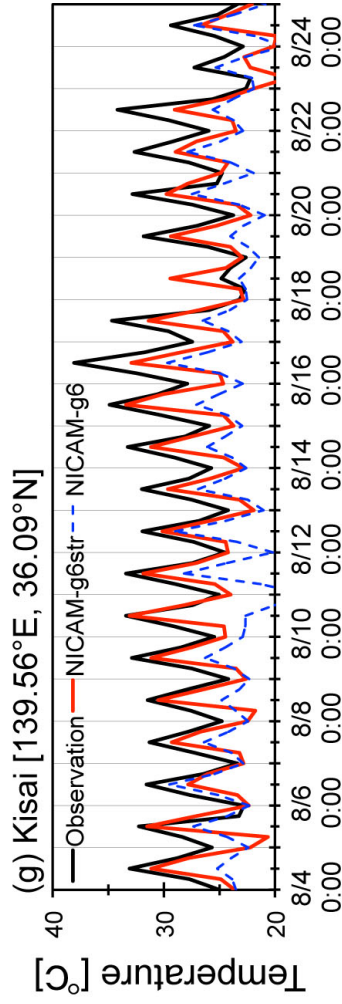
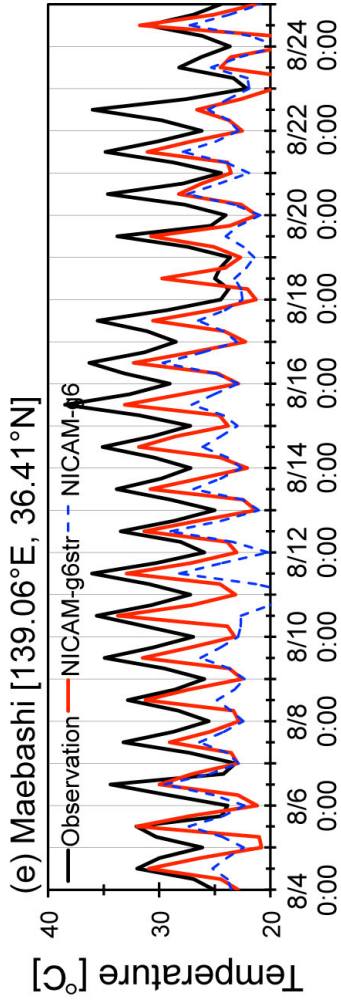
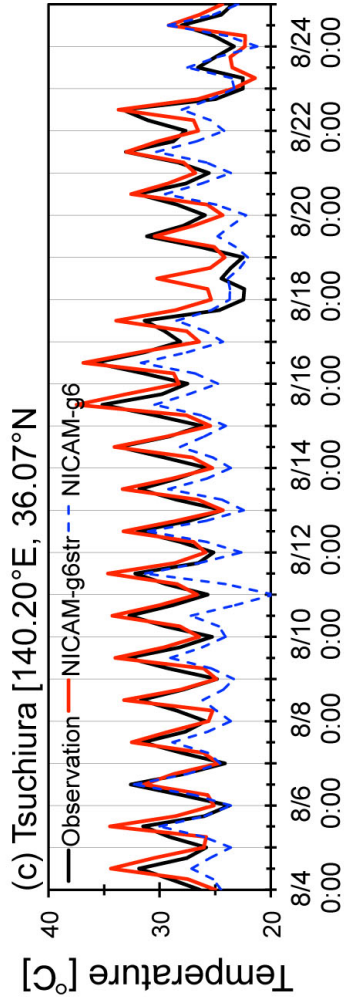
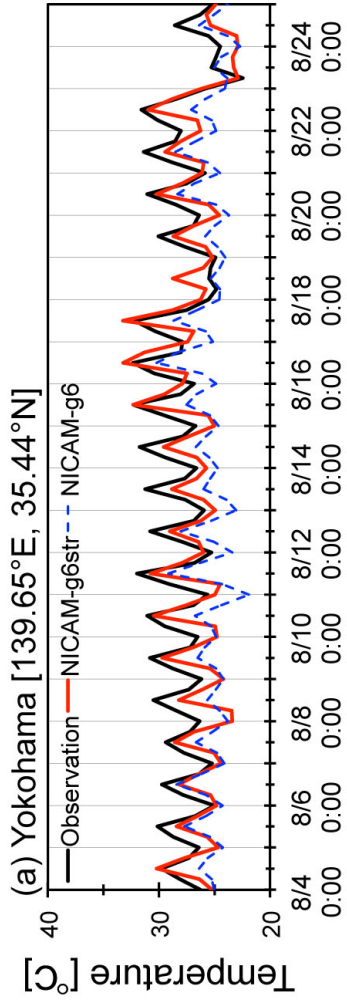


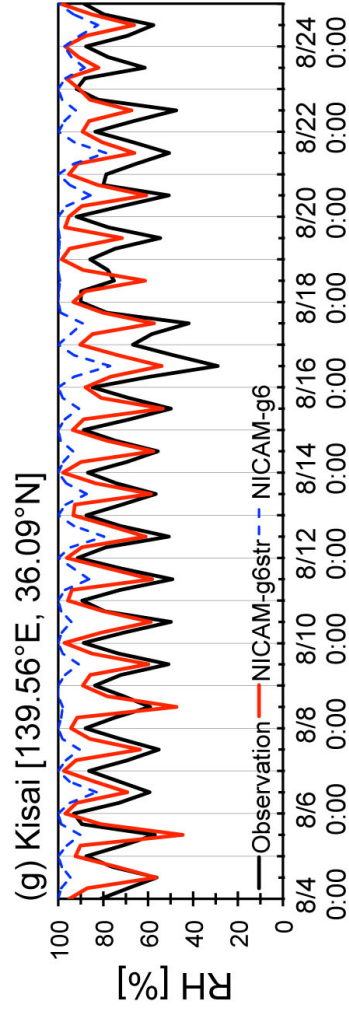
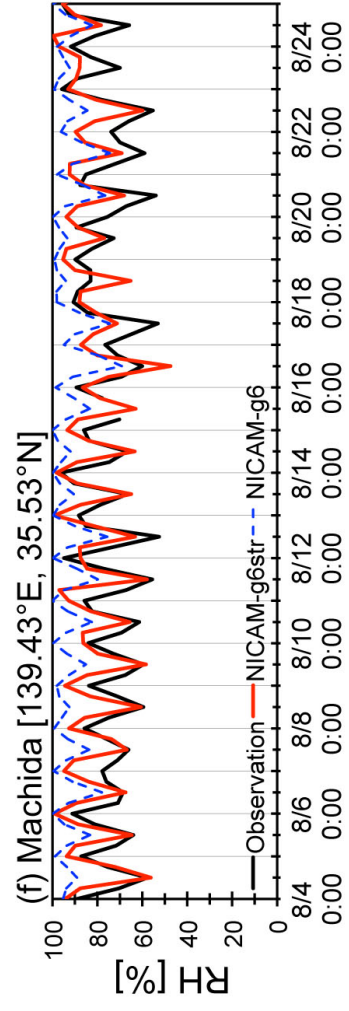
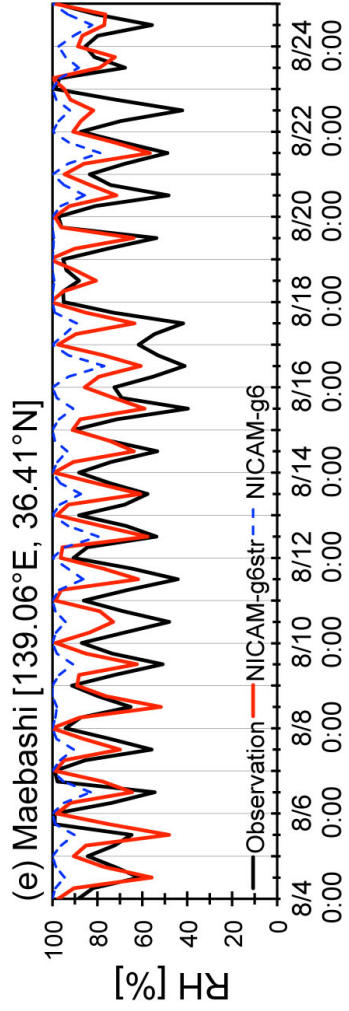
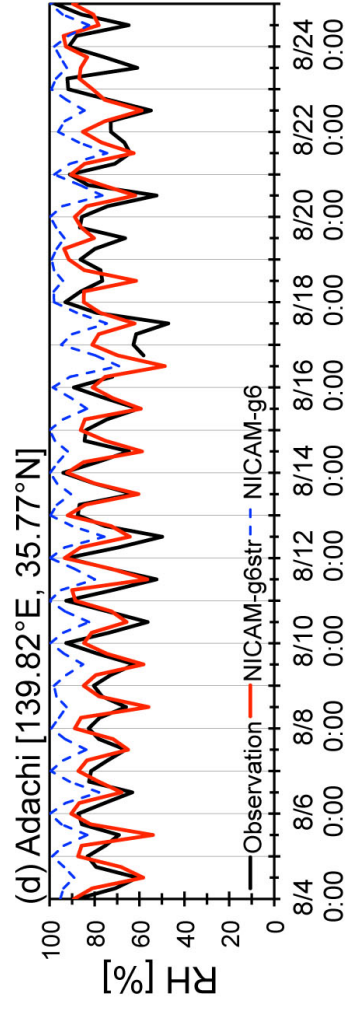
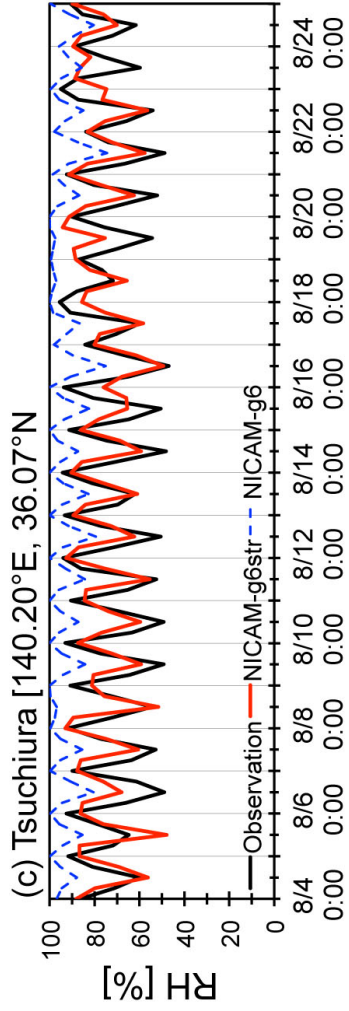
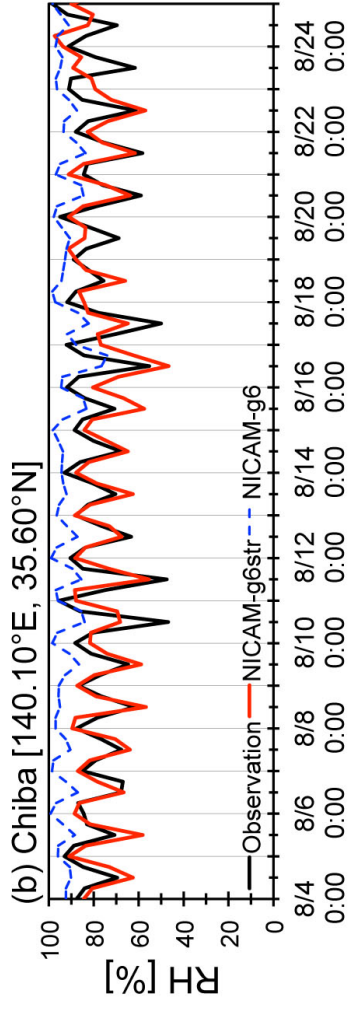
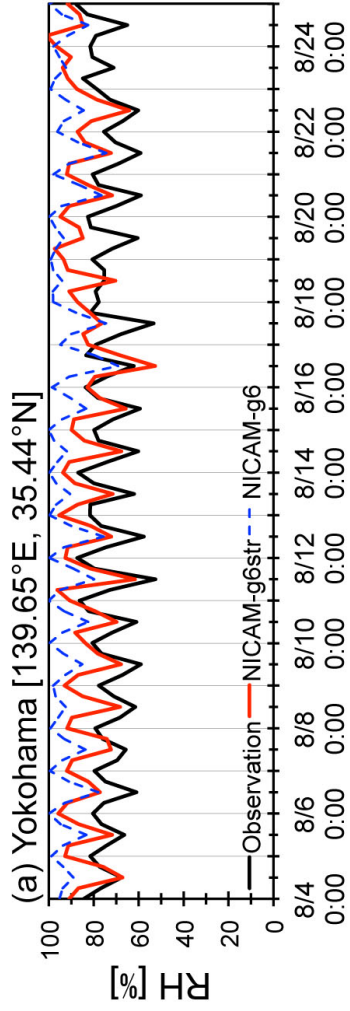
NICAM-g6str



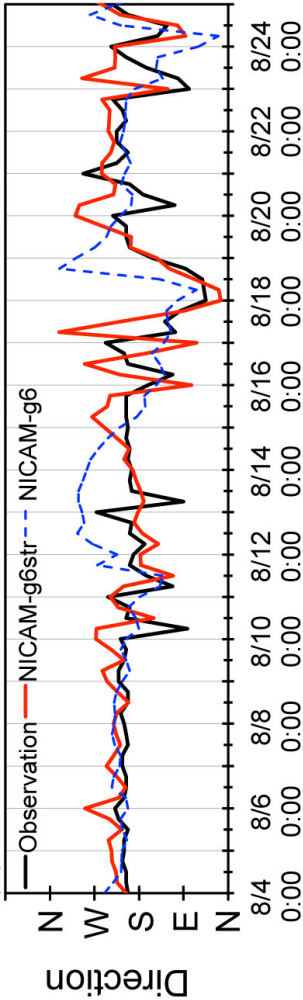
NICAM-g6



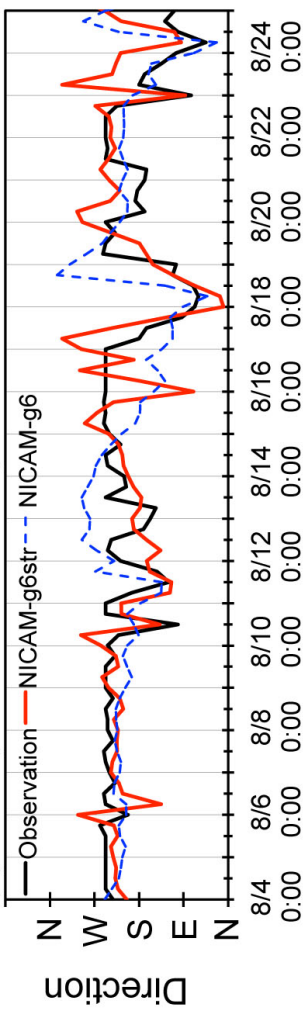




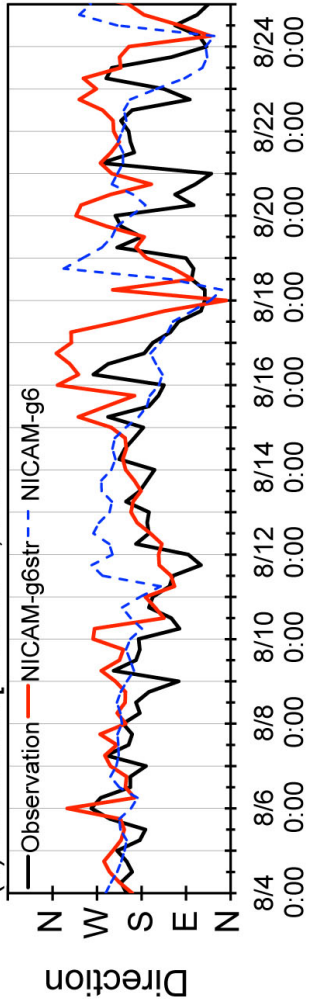
(a) Yokohama [139.65°E, 35.44°N]



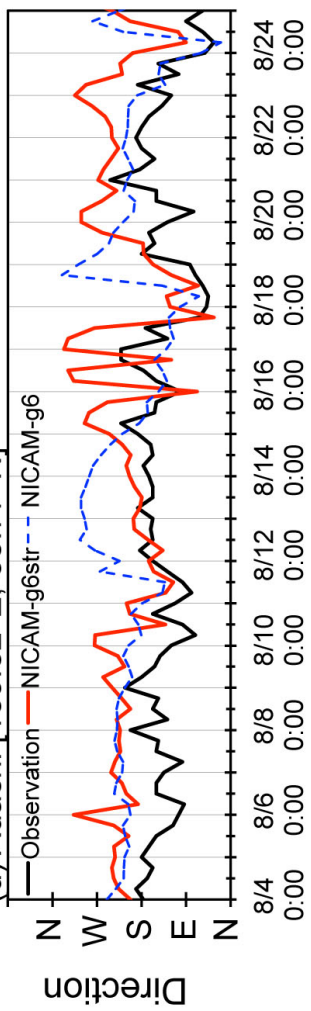
(b) Chiba [140.10°E, 35.60°N]



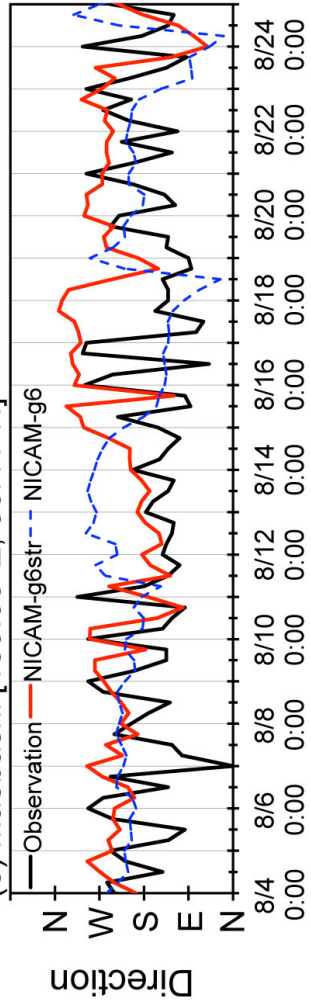
(c) Tsuchiura [140.20°E, 36.07°N]



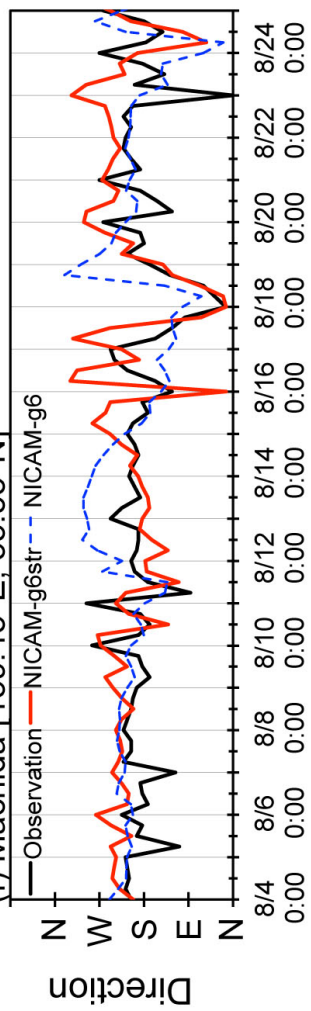
(d) Adachi [139.82°E, 35.77°N]



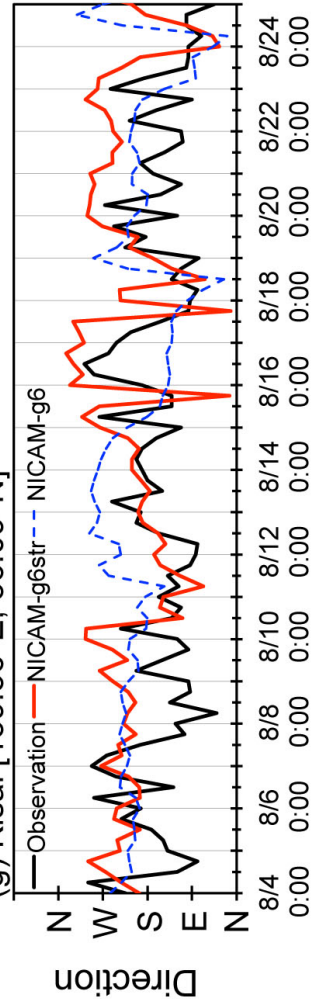
(e) Maebashi [139.06°E, 36.41°N]

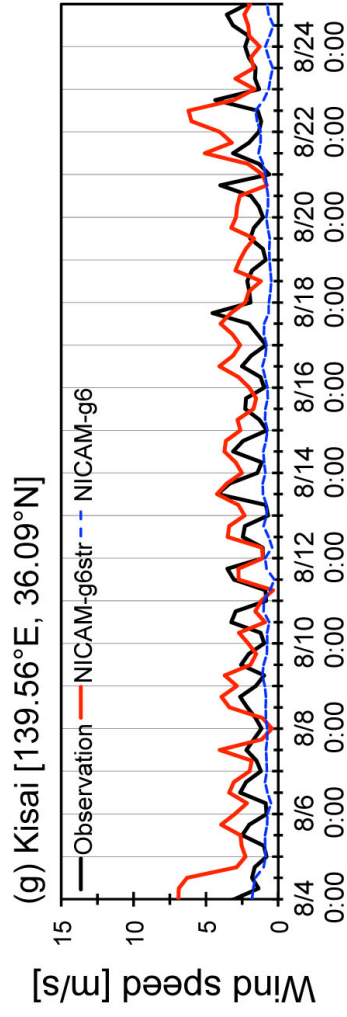
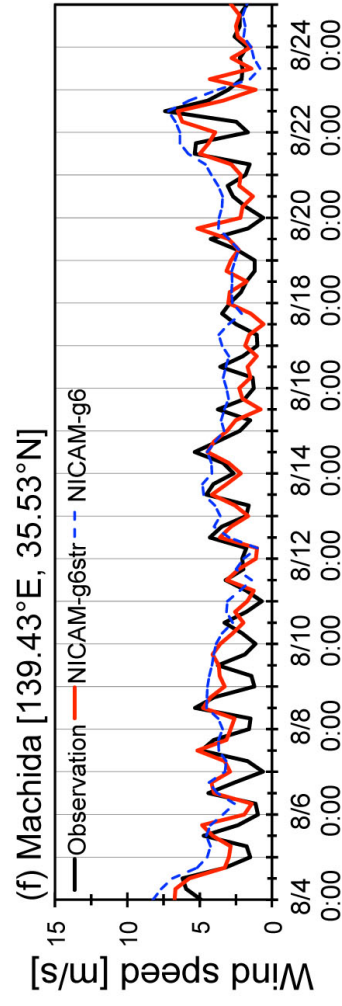
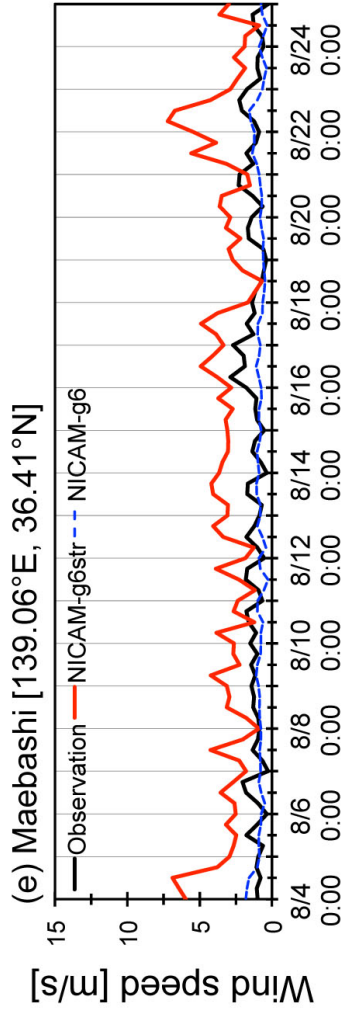
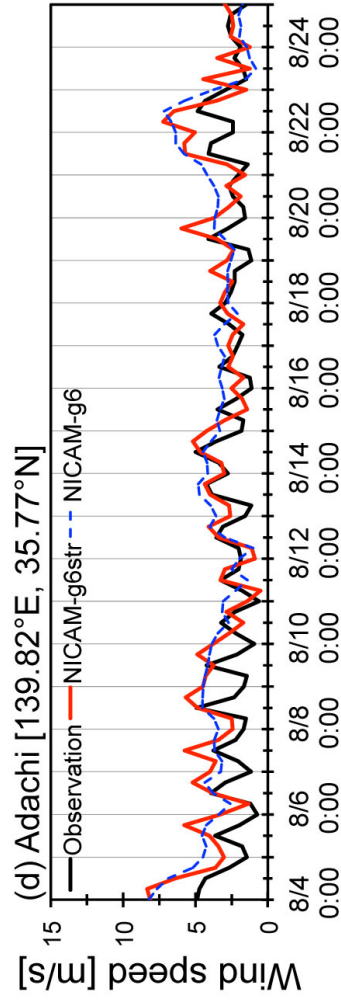
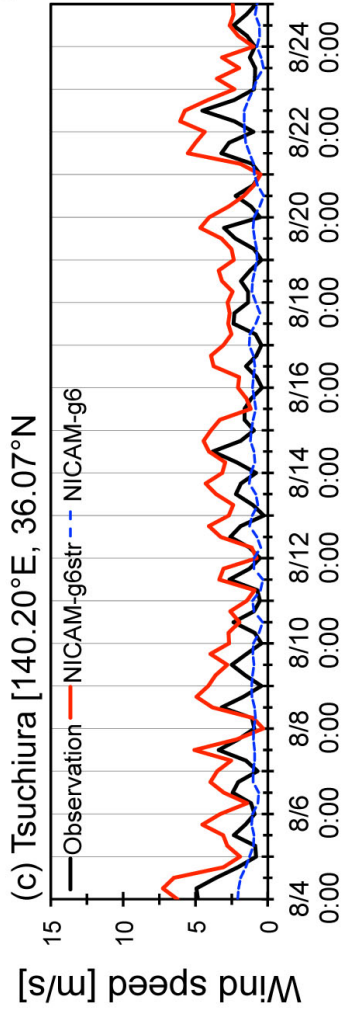
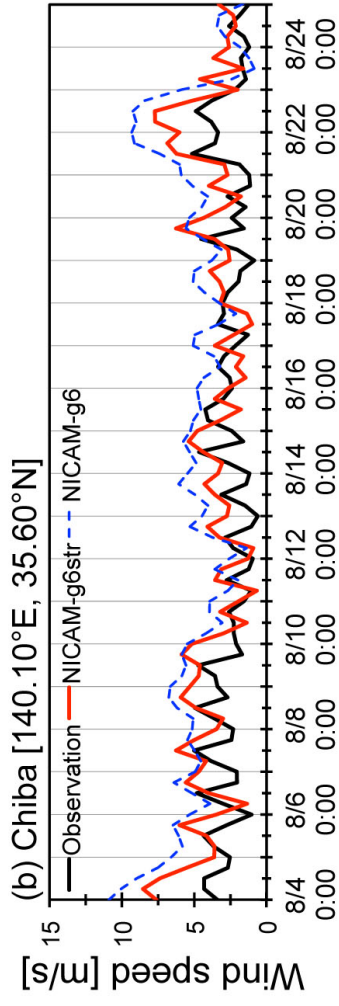
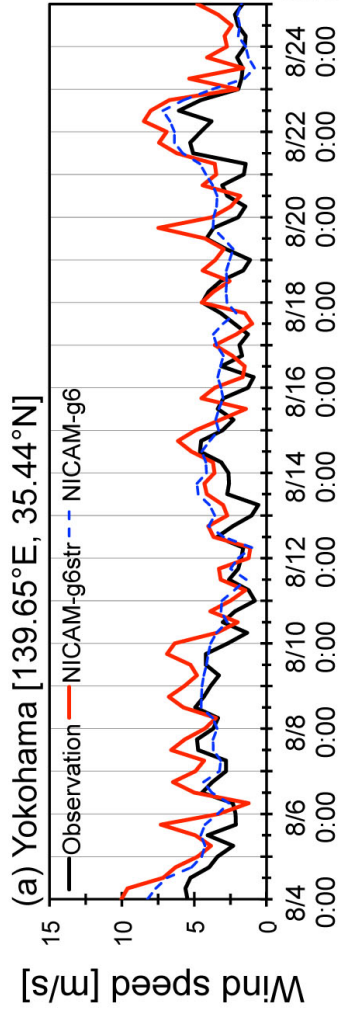


(f) Machida [139.43°E, 35.53°N]

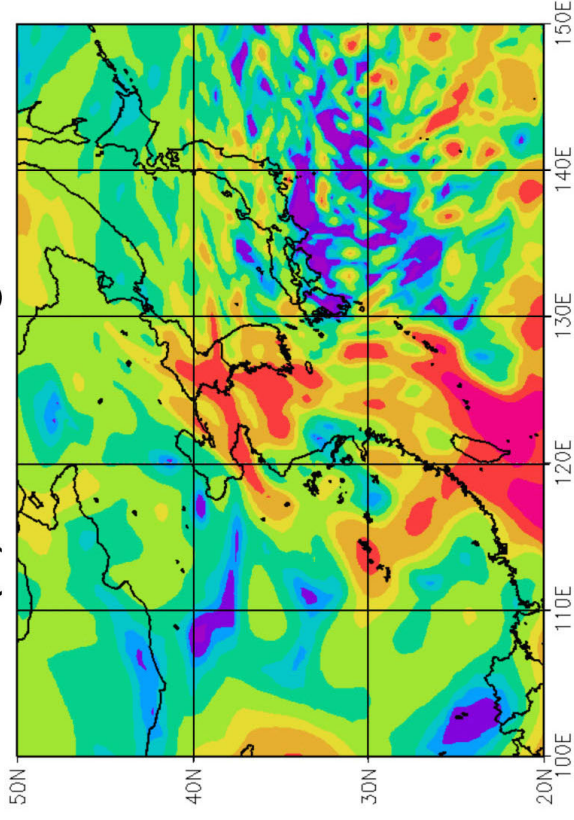


(g) Kisai [139.56°E, 36.09°N]

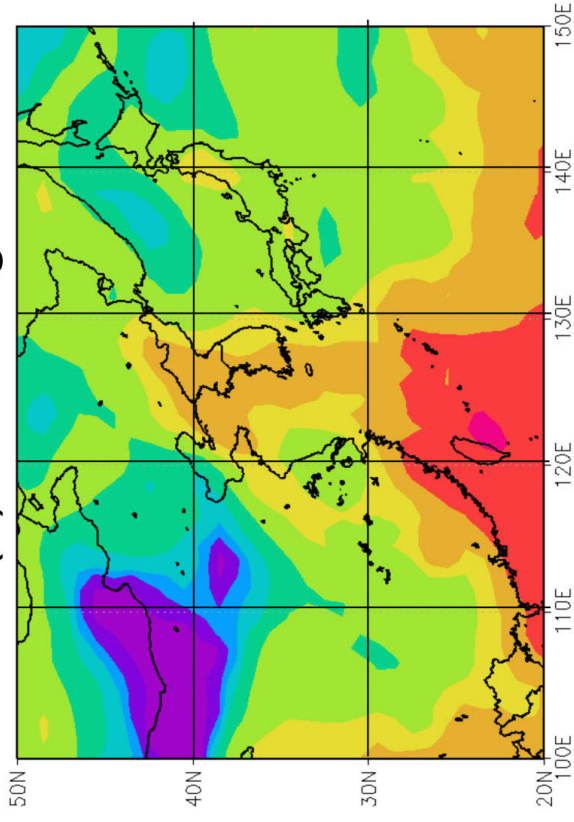




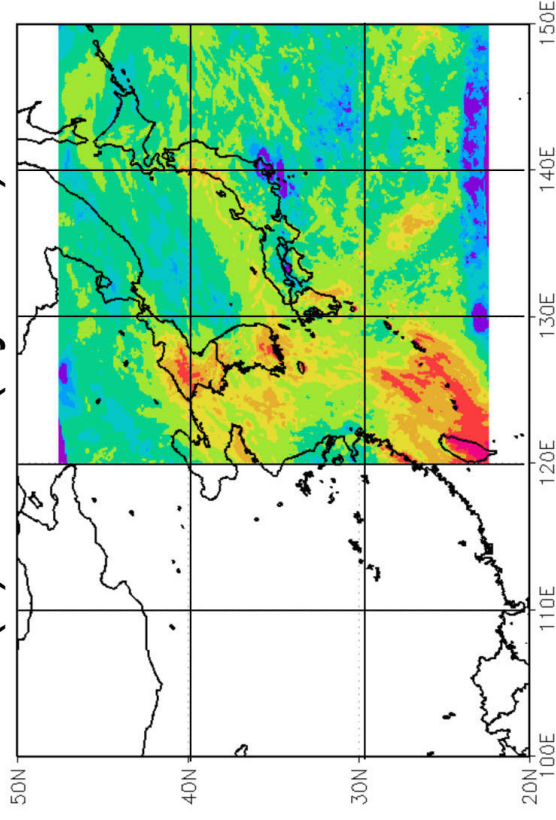
(a) NICAM-g6str



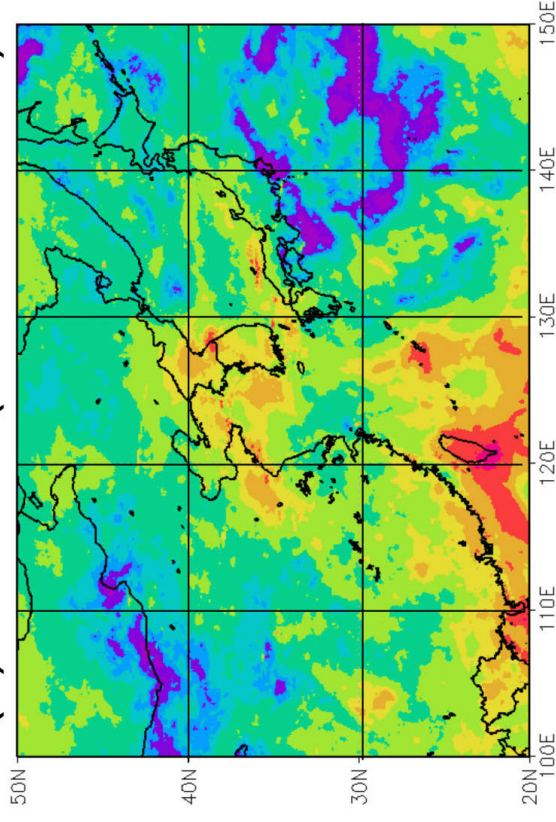
(b) NICAM-g6

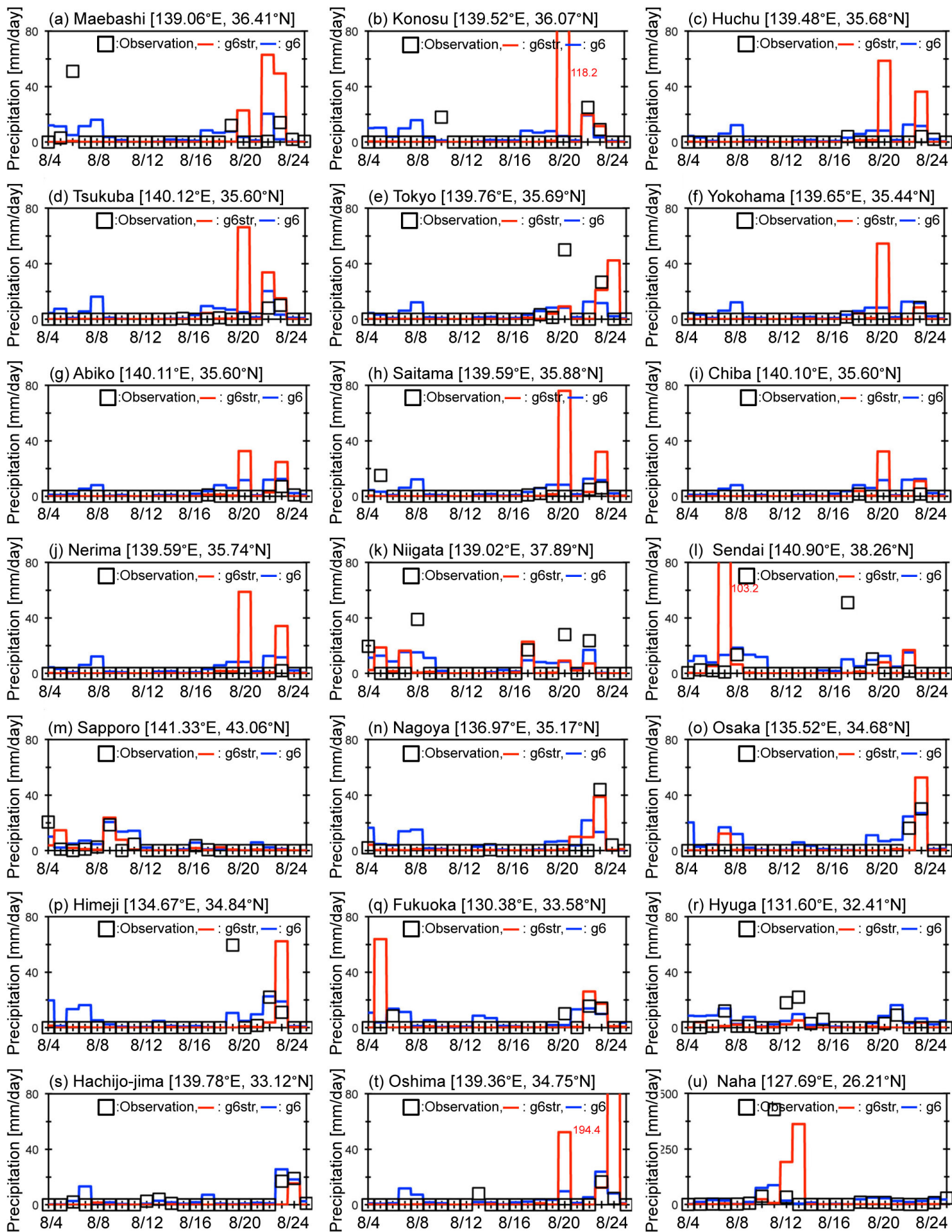


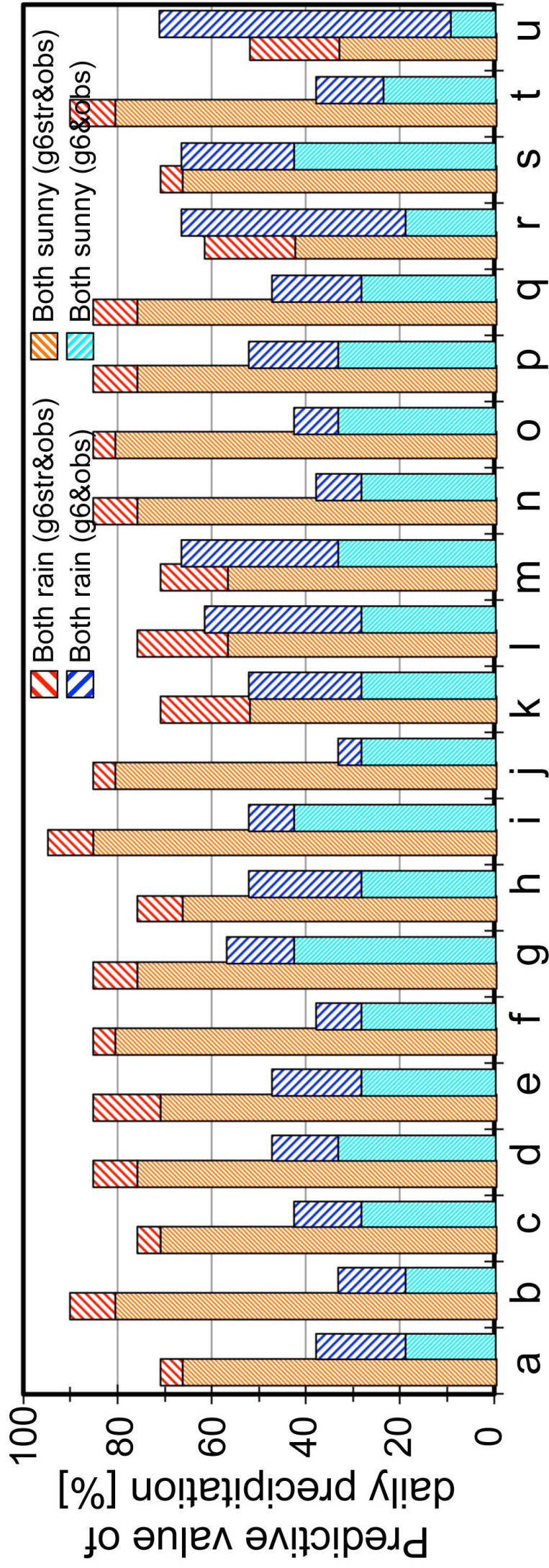
(c) MSM (by JMA)



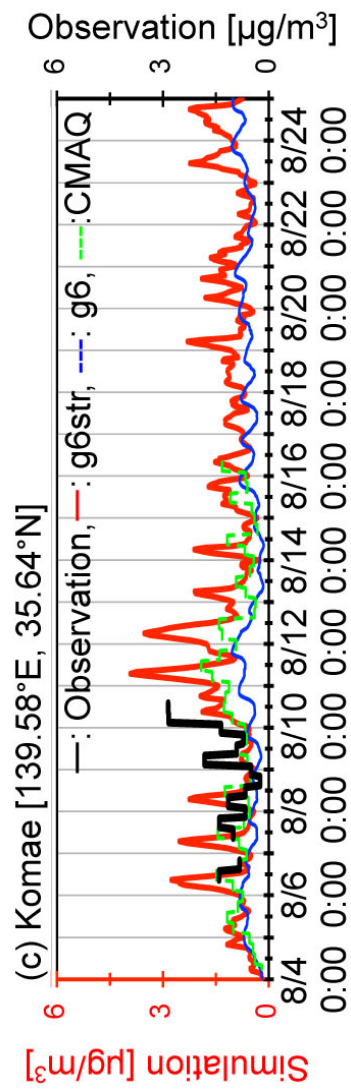
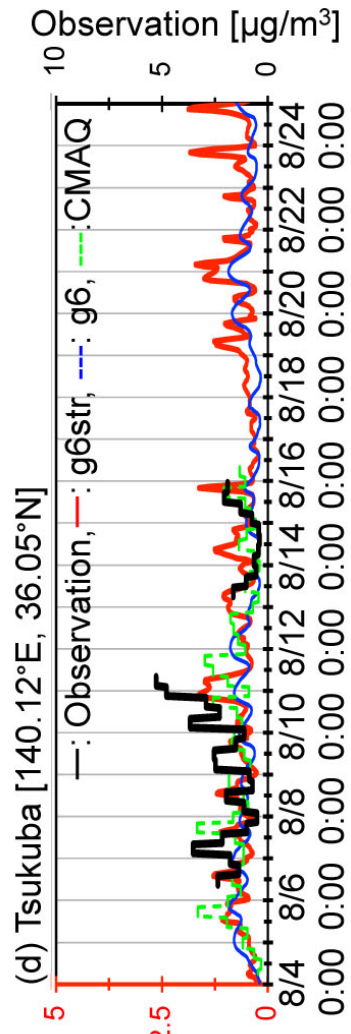
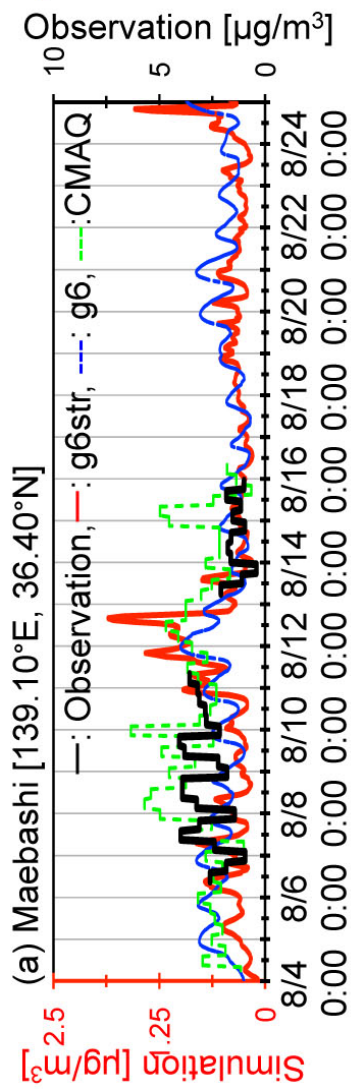
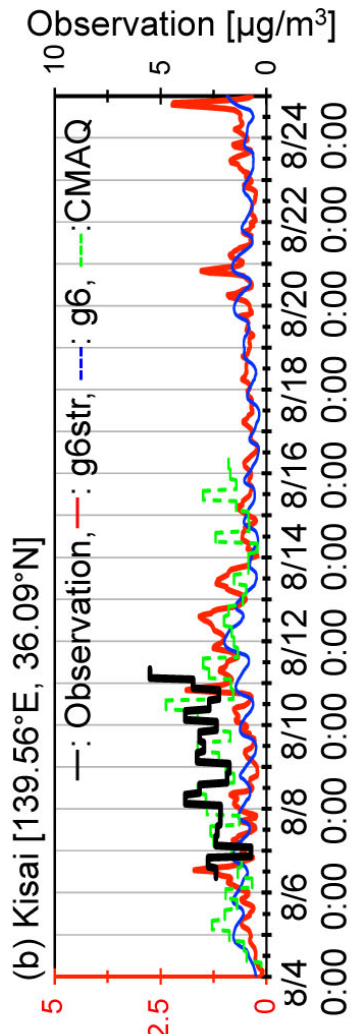
(d) GSMaP (multi-satellite)

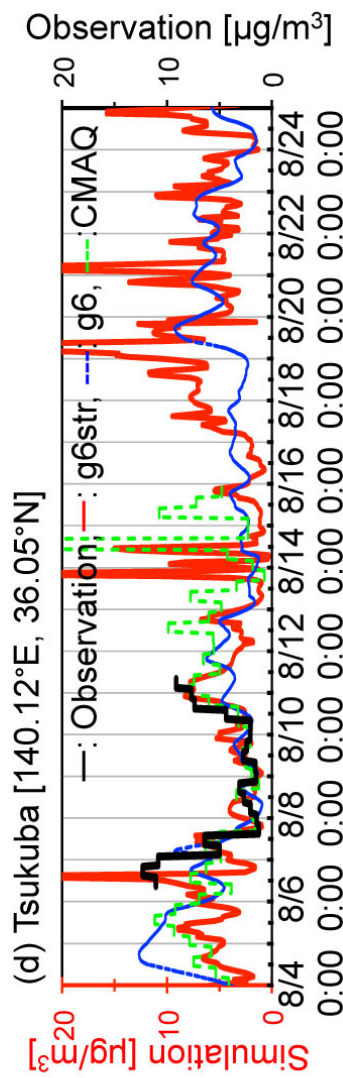
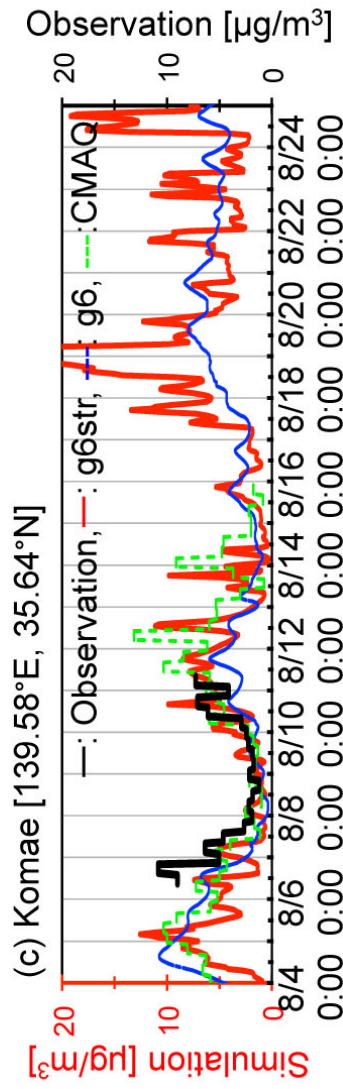
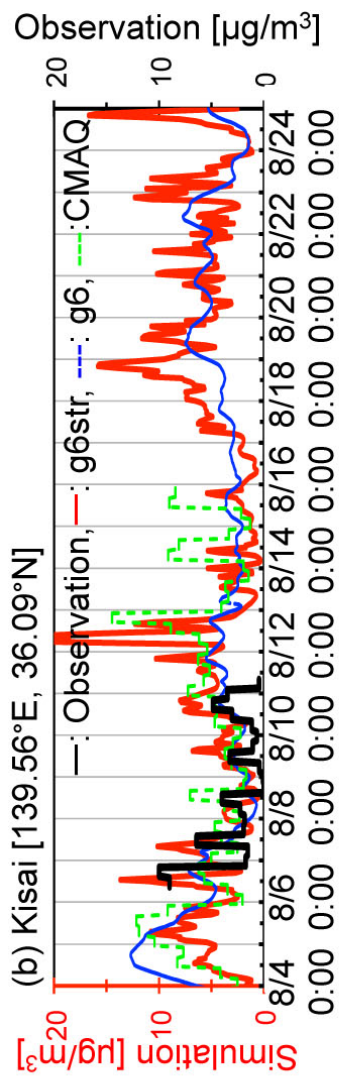
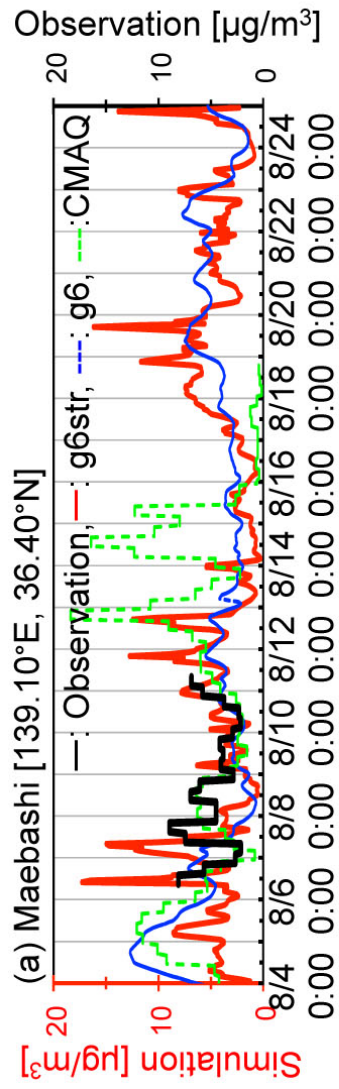


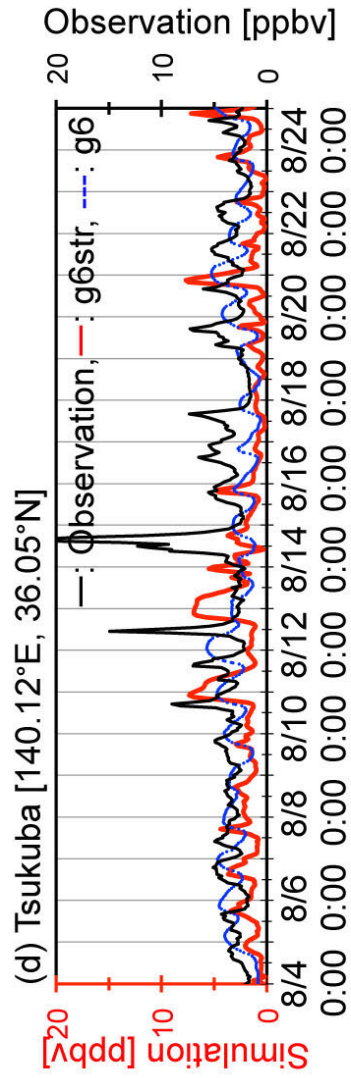
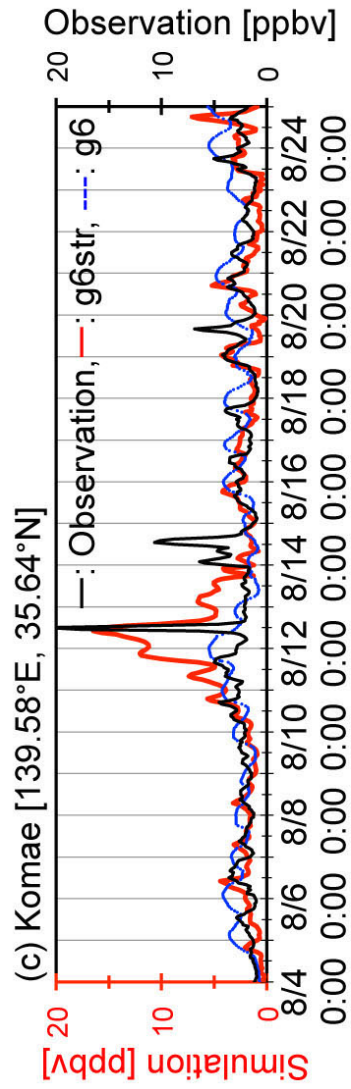
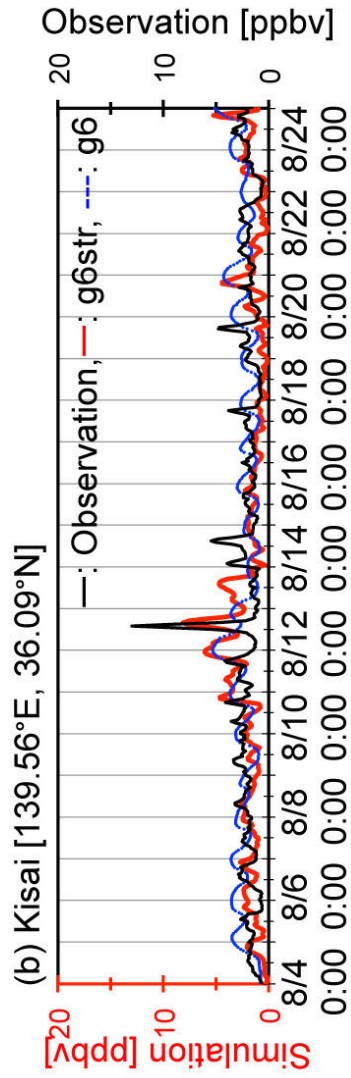
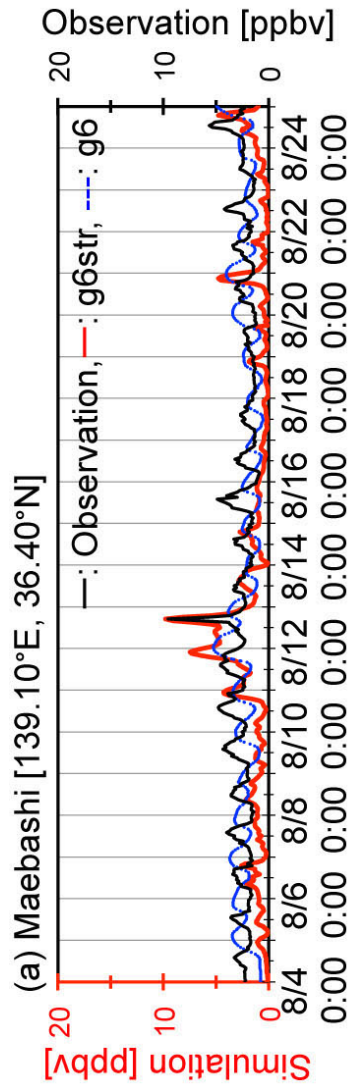




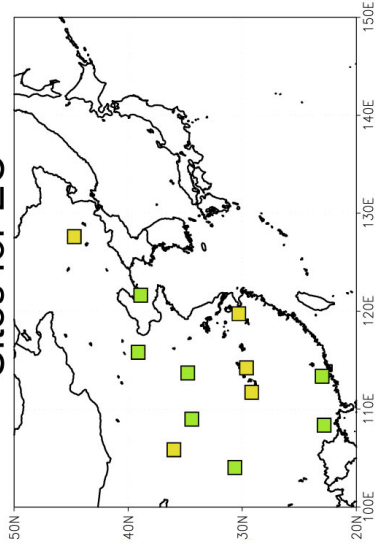
Sites (corresponding to the sites shown in Figure 9)



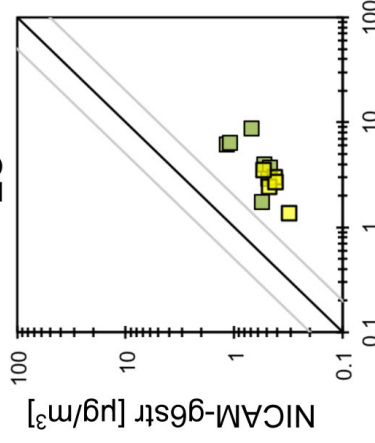




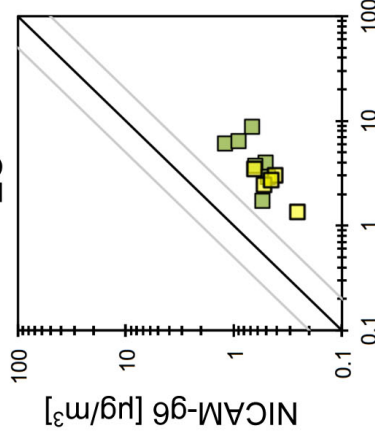
Sites for EC



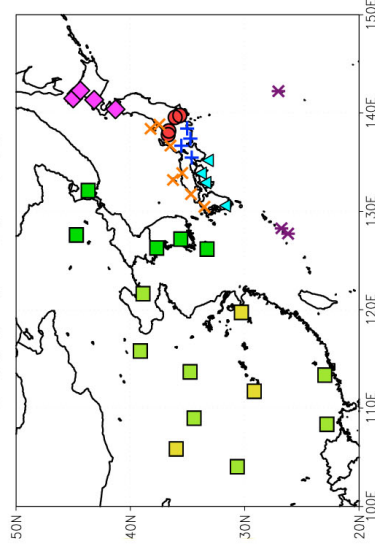
EC



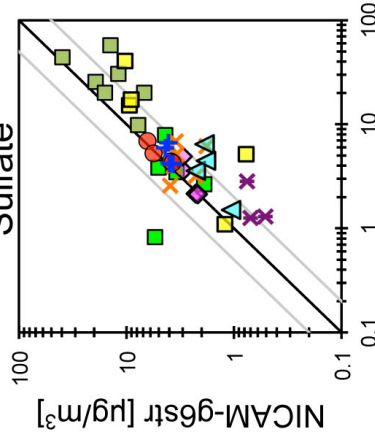
EC



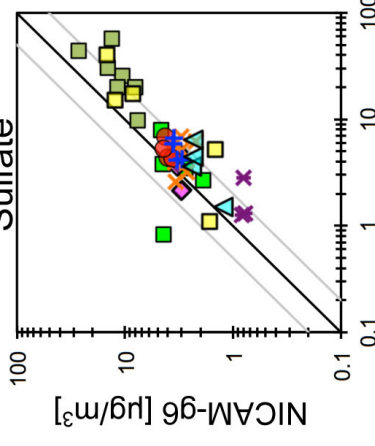
Sites for sulfate



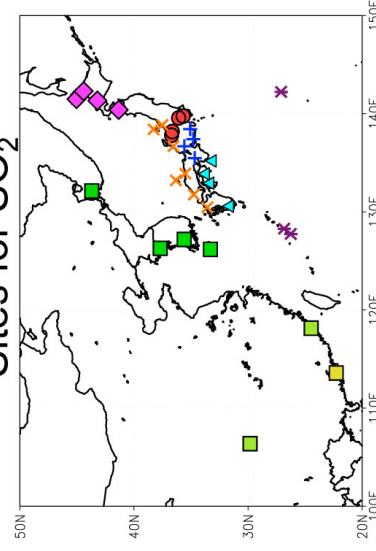
Sulfate



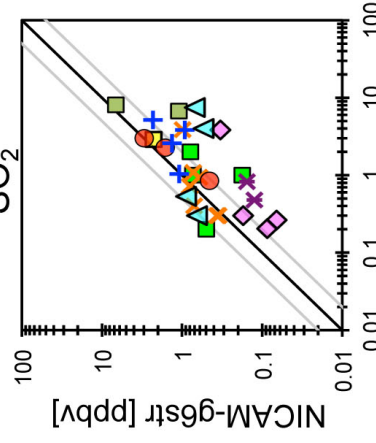
Sulfate



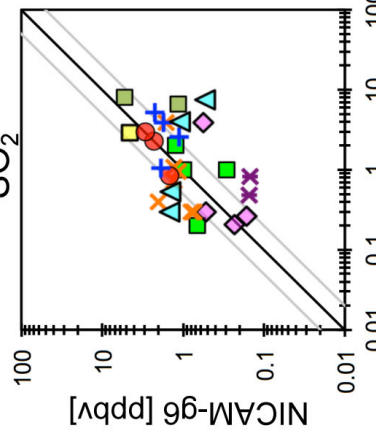
Sites for SO₂

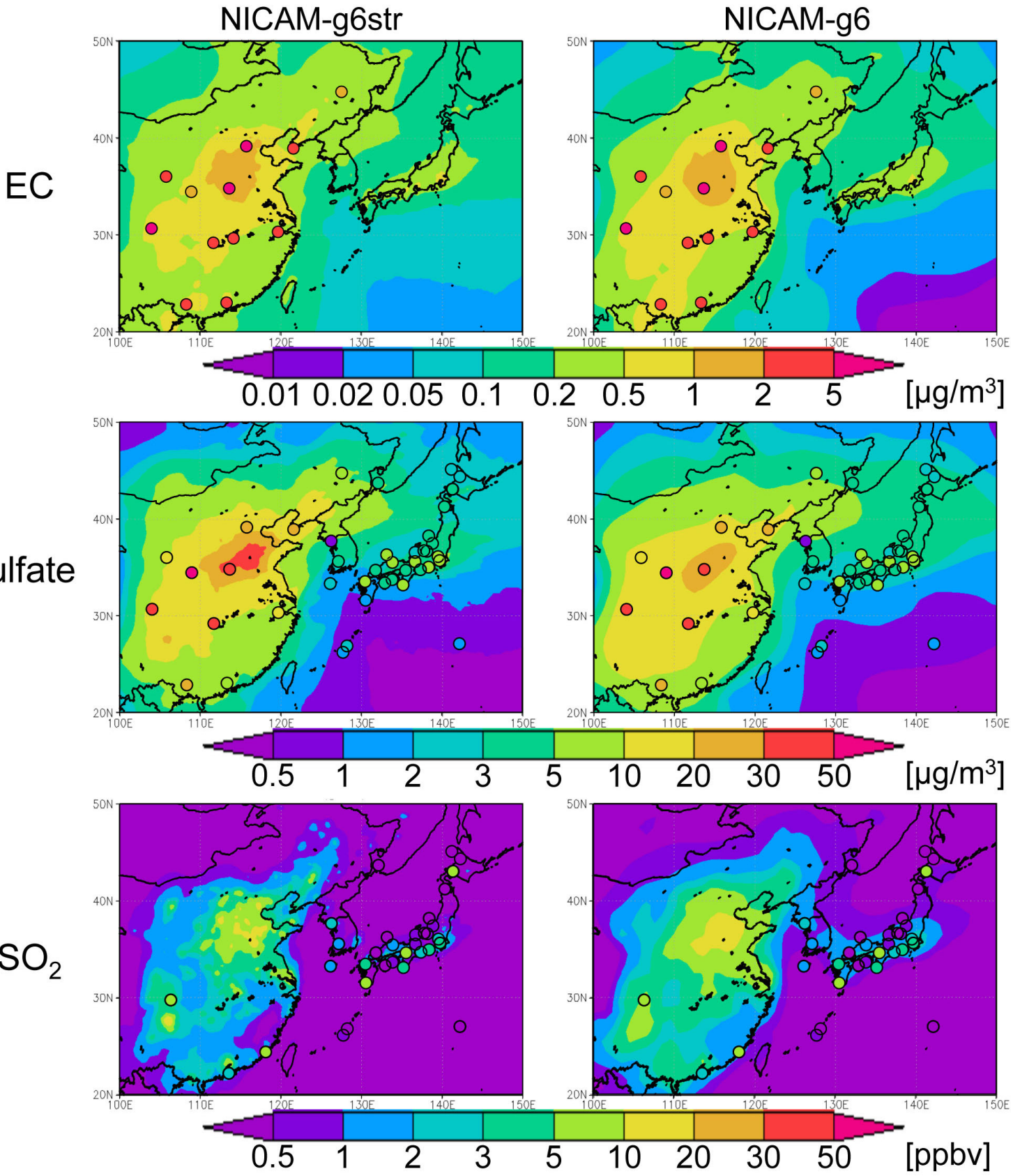


SO₂

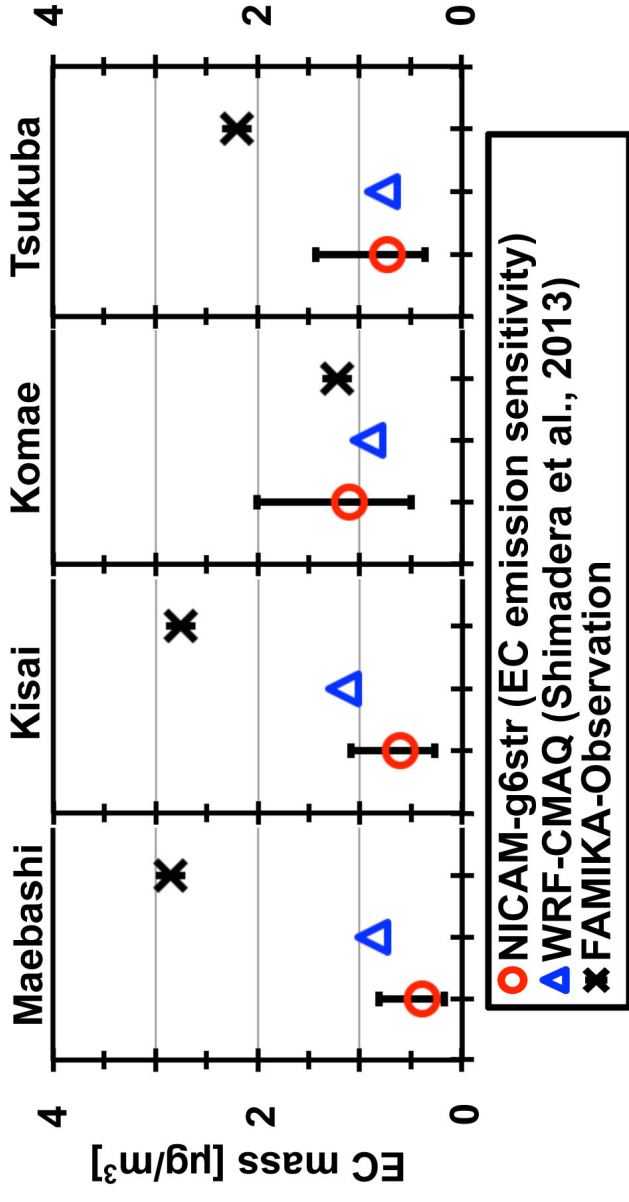


SO₂

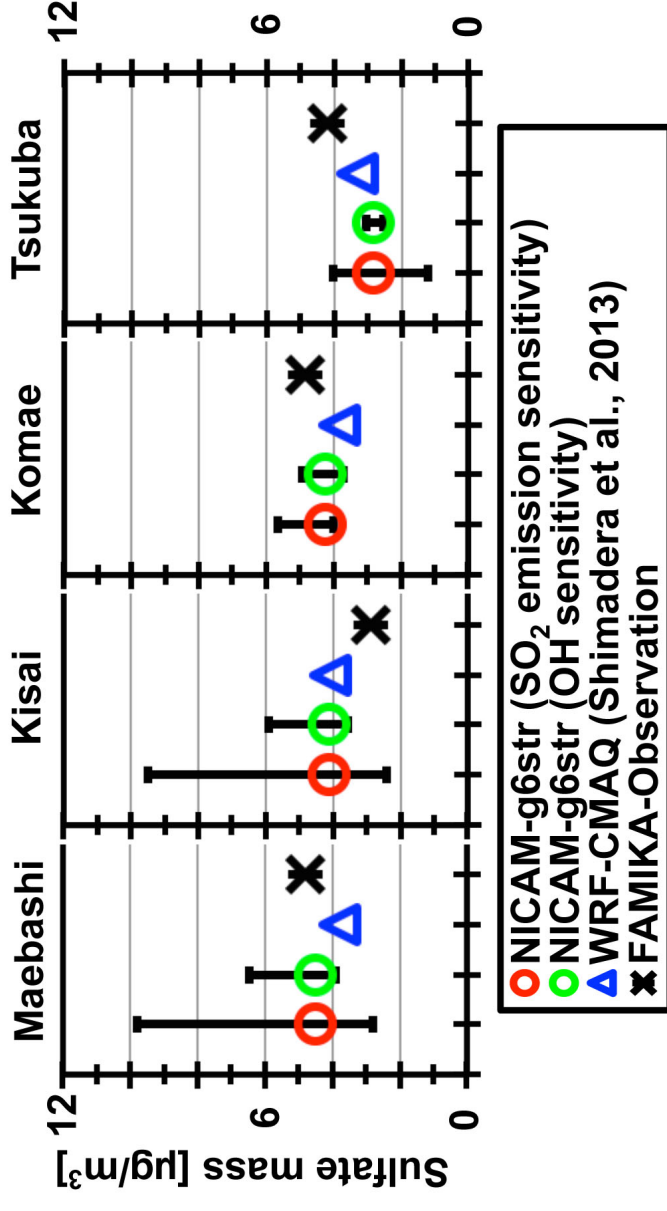


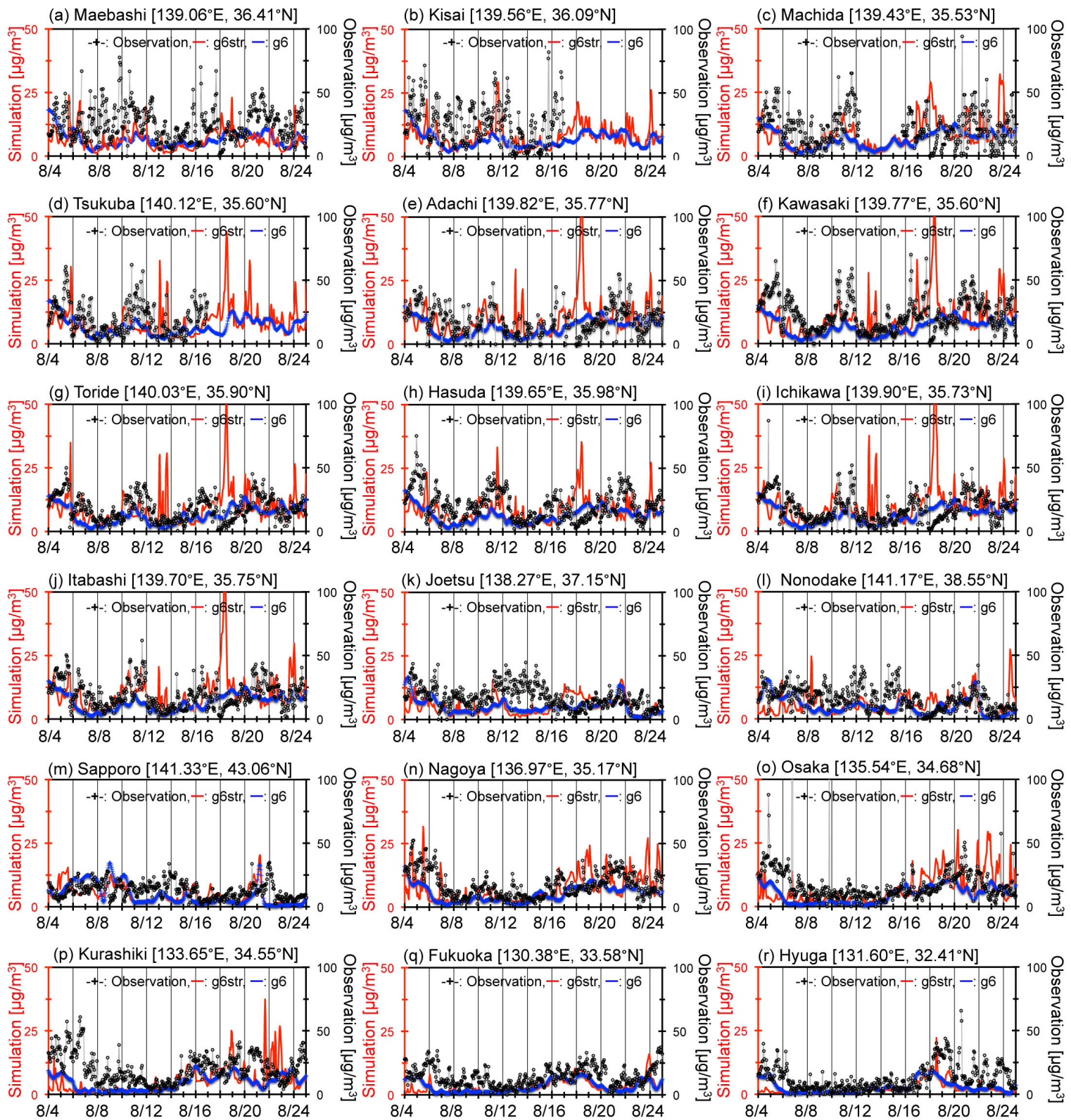


(a) EC mass concentration at FAMIKA sites

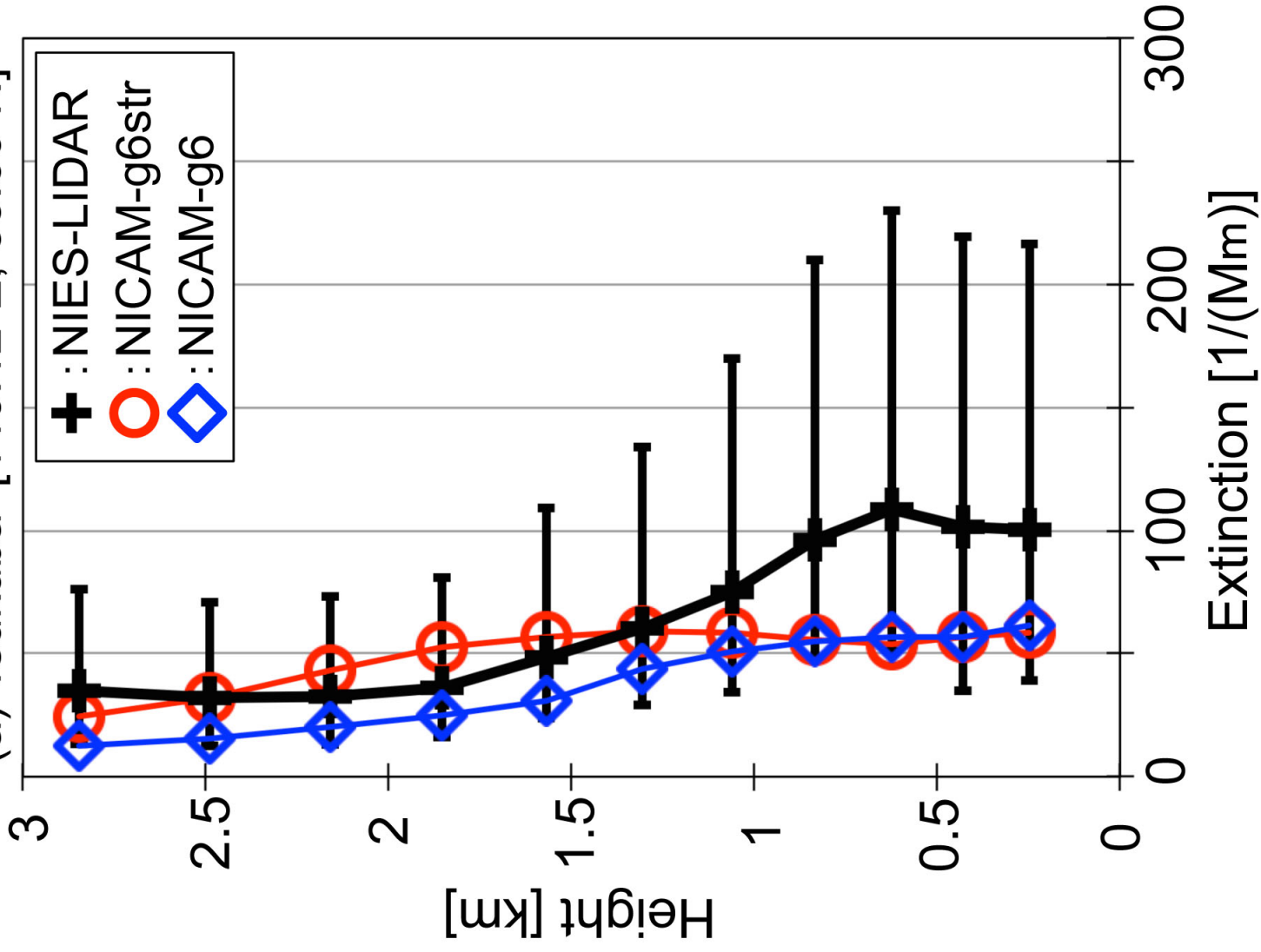


(b) Sulfate mass concentration at FAMIKA sites





(a) Tsukuba [140.12°E, 35.60°N]



(b) Chiba [140.10°E, 35.60°N]

